Plasmodium NEK1 coordinates MTOC organisation and kinetochore attachment during rapid mitosis in male gamete formation

Mohammad Zeeshan[1#], Ravish Rashpa[2#], David J. Ferguson[3,4], George Mckeown[1], Raushan Nugmanova[5], Amit K. Subudhi[5], Raphael Beyeler[6], Sarah L. Pashley[1], Robert Markus[1], Declan Brady[1], Magali Roques[6], Andrew R. Bottrill[7], Andrew M. Fry[8], Arnab Pain[5], Sue Vaughan[3], Anthony A. Holder[9], Eelco C. Tromer[10], Mathieu Brochet[2]*, Rita Tewari[1]*

[1]University of Nottingham, School of Life Sciences, Nottingham, UK.
[2]University of Geneva, Faculty of Medicine, Geneva, Switzerland.
[3]Oxford Brookes University, Department of Biological and Medical Sciences, Oxford, UK
[4]University of Oxford, John Radcliffe Hospital, Nuffield Department of Clinical Laboratory Science, Oxford, United Kingdom.
[5]Pathogen Genomics Group, Bioscience Program, BESE Division, King Abdullah University of Science and Technology (KAUST), Thuwal, Kingdom of Saudi Arabia
[6]Institute of Cell Biology, University of Bern, Bern, Switzerland.
[7]School of Life Sciences, Gibbet Hill Campus, University of Warwick, Coventry, UK
[8]Department of Molecular and Cell Biology, University of Leicester, Leicester, UK
[9]Malaria Parasitology Laboratory, The Francis Crick Institute, London, UK
[10]Cell Biochemistry, Groningen Biomolecular Sciences and Biotechnology Institute, Faculty of Science and Engineering, University of Groningen, Groningen, The Netherlands

* Rita.Tewari@nottingham.ac.uk–Lead contact; Mathieu.Brochet@unige.ch
[#] These authors contributed equally

Short title: *Plasmodium* NEK1 in MTOC organisation

Abstract

Mitosis is an important process in the cell cycle required for cells to divide. Never in mitosis (NIMA)-like kinases (NEKs) are regulators of mitotic functions in diverse organisms. *Plasmodium*, the causative agent of malaria is a divergent unicellular haploid eukaryote with some unusual features in terms of its mitotic and nuclear division cycle that presumably facilitate proliferation in varied environments. For example, during the sexual stage of male gametogenesis within the mosquito host, an atypical rapid closed endomitosis is observed. Three rounds of genome replication from 1N to 8N and successive cycles of multiple spindle formation and chromosome segregation occur within eight minutes followed by karyokinesis to generate haploid gametes.

Our previous *Plasmodium* kinome screen identified four *Nek* genes, of which two, NEK2 and NEK4, are required for meiosis. NEK1 is likely to be essential for mitosis in asexual blood stage schizogony in the vertebrate host, but its function during male gametogenesis is unknown. Here, we study NEK1 location and function, using live cell imaging, ultrastructure expansion microscopy (U-ExM) and electron microscopy, together with conditional gene knockdown and proteomic approaches. We report spatiotemporal NEK1 location in real-time, coordinated with microtubule organising centre (MTOC) dynamics during the unusual mitoses at various stages of the *Plasmodium* life cycle. Knockdown studies reveal NEK1 to be an essential component of the MTOC in male cell differentiation, associated with rapid mitosis, spindle formation and kinetochore attachment. These data suggest that Plasmodium NEK1 kinase is an important component of MTOC organisation and essential regulator of chromosome segregation during male gamete formation.

Introduction

Mitosis has a key role in the eukaryotic cell cycle when the cell divides and produces daughter cells. During mitosis, centrosomes act as microtubule organising centres (MTOCs) coordinating spindle dynamics with chromosome congression and segregation. They also act as signalling hubs for regulators of mitosis, including cyclin-dependent kinases (CDKs), and Aurora, Polo and NIMA-related (NEK) kinases (Arquint et al., 2014). NIMA (Never In Mitosis)-related kinases were first identified in *Aspergillus nidulans* during a screen for regulators of mitosis (Oakley and Morris, 1983), and members of this family are found in a wide range of eukaryotes where they are crucial for cell cycle progression and microtubule organization (Fry et al., 2017; Fry et al., 2012; O'Connell et al., 2003).

Budding and fission yeast express a single NEK kinase (Grallert and Hagan, 2002), but the family is expanded to 11 members in mammals, which may reflect the increased complexity of microtubule-dependent processes (Fry et al., 2017). Several NEKs are essential to form functional cilia and flagella in mammals and other organisms, including *Chlamydomonas, Trypanosoma* and *Tetrahymena* (Mahjoub et al., 2004; Pradel et al., 2006; Wloga et al., 2006). Other NEKs are more directly implicated in mitotic cell division, with defects in NEK expression likely to contribute to aberrant chromosome segregation in cancer cells (Bachus et al., 2022; Fry et al., 2017).

NEKs are located at MTOCs in many organisms, including Aspergillus, yeast and human cells (Bachus et al., 2022; Fry et al., 2017; Quarmby and Mahjoub, 2005). Of the eleven mammalian NEKs, NEK2, NEK6, NEK7 and NEK9 localise to centrosomes, playing roles in mitotic spindle assembly (Moniz et al., 2011). The centrosome is an MTOC in mammalian cells composed of two microtubule-based barrel-shaped structures, termed centrioles, surrounded by a meshwork of mainly coiled-coil proteins that form the pericentriolar matrix (Avidor-Reiss and Fishman, 2019; Bettencourt-Dias and Glover, 2007). The MTOC equivalent in yeast, the spindle pole body (SPB), lacks centrioles and is normally embedded in the nuclear membrane (Kilmartin, 2014). The SPB largely controls spindle dynamics during the so-called closed mitosis that occurs in these organisms, since the nuclear envelope

does not break down. Here, the SPB acts not only to nucleate and anchor microtubules, but also to form a signalling hub for cell cycle-dependent kinases and phosphatases (Arquint et al., 2014).

Plasmodium, the causative agent of malaria, is an alveolate Apicomplexa parasite that exhibits extensive plasticity in mitosis and cell division during its life cycle, with proliferation within the two hosts, the *Anopheles* mosquito, and a vertebrate. These parasites display some atypical aspects of cell division, for example in terms of cell cycle, MTOC organisation, chromosome segregation and nuclear division, presumably to facilitate genome replication and cell proliferation in the varied environments (Guttery et al., 2022; Roques et al., 2023; Voss et al., 2023). In a mammalian host, asexual division (schizogony) occurs first in hepatocytes followed by cyclic schizogony and replication in erythrocytes (the blood stage); parasites progress through ring, trophozoite and the multinucleate schizont stage, finally releasing merozoites to infect new cells. In the schizont, division occurs by closed mitosis with asynchronous division of individual nuclei, and cytokinesis only occurs at the end of the schizont stage. In the mosquito, sexual stages occur within the gut. Male and female gametes (gametogenesis) are produced from gametocytes in the blood meal, and following fertilisation the zygote develops into a motile ookinete in which meiosis begins. The ookinete migrates through the mosquito gut wall and forms an oocyst, where further asexual replication occurs to produce the sporozoites that migrate to the mosquito's salivary glands prior to transfer to the vertebrate host in a further blood meal. During male gamete formation (microgametogenesis) mitosis is unconventional: three-fold genome replication from 1N to 8N is accompanied by three rapid successive cycles of spindle formation and chromosome segregation (Mitosis I, II and III) and followed by subsequent karyokinesis, all within eight minutes (Guttery et al., 2022; Sinden, 1991; Sinden et al., 2010). Neither centrosomes nor centrioles have been observed during the proliferative schizont stages within the mammalian host (Li et al., 2022). *Plasmodium* contains a bipartite MTOC, that consists of a cytoplasmic part (outer MTOC) and a nuclear component (inner MTOC). During erythrocytic schizogony, the MTOC is also known as the centriolar plaque and contains an acentriolar cytoplasmic MTOC and a nuclear component called the intranuclear body (Liffner et al., 2023; Simon et al., 2021; Voss et al., 2023). The centriolar plaque is located at the nuclear membrane during mitosis

and appears morphologically more similar to the yeast SPB than the human centrosome (Arnot et al., 2011). During male gametogenesis, the bipartite MTOC has a cytoplasmic centriolar part where basal bodies are organised, and an inner nuclear component, called a nuclear pole (Hair et al., 2023; Sinden, 1991; Zeeshan et al., 2022a; Zeeshan et al., 2023). A centriole is found in the life cycle only during male gametogenesis and is associated with formation of the flagellated gamete (Sinden, 1991; Sinden et al., 2010).

Functional analysis of the *Plasmodium* kinome by gene deletion, phylogenetic analysis and phenotypic approaches identified many unusual features of the cell cycle and revealed that the molecules that control it may differ significantly from those other model eukaryotes (Solyakov et al., 2011; Tewari et al., 2010). Strikingly, there are no genes for polo-like kinases, typical cyclins, or many components of the anaphase promoting complex (Roques et al., 2015; Solyakov et al., 2011; Tewari et al., 2010; Wall et al., 2018). Genes for phosphatases involved in mitosis, such as Cdc25 and Cdc14, are absent (Guttery et al., 2014b; Solyakov et al., 2011; Tewari et al., 2010). However, four NIMA-like kinases were identified in *Plasmodium,* and all are expressed most highly in gametocytes (Solyakov et al., 2011; Tewari et al., 2010). These kinases have been named NEK1 to NEK4, but they are not directly analogous to mammalian NEK1 to NEK4. Previous gene knockout studies showed that *Plasmodium* NEK2 and NEK4 are required for zygote differentiation and meiosis, but not for mitotic division of parasite cells in mammalian red blood cells (Reininger et al., 2005; Reininger et al., 2009), whereas NEK1 is likely essential for blood stage schizogony and proliferation (Dorin-Semblat et al., 2011; Tewari et al., 2010). It has been shown that the recombinant PfNEK1 is able to autophosphorylate, and the FFXT consensus motif usually found in the NEK family is substituted by an SMAHS motif (Dorin et al., 2001). In addition PfNEK1 is able to phosphorylate PfMAP2 in vitro and hence may be involved in the modulation of MAPK pathway, in the absence of classical MEKK-MEK-MAPK signalling, which is missing from *Plasmodium* ((Dorin-Semblat et al., 2011; Dorin et al., 2001). Another study of asexual erythrocytic schizogony in *Plasmodium* demonstrated the inhibitory role of Hesparadin, a human aurora kinase inhibitor, targeting the kinase domain of PfNEK1 (Morahan et al., 2020).

The role of NEK1 in centrosome splitting, a step necessary for bipolar spindle assembly, and the formation of daughter cells in asexual stages has been demonstrated elegantly in *Toxoplasma gondii*, a related apicomplexan species (Chen and Gubbels, 2013).

Most information on NEKs was obtained using asexual stages of the parasite and nothing is known about the spatiotemporal dynamics and function of NEK1 during the rapid mitoses of male gametogenesis. Here, using the rodent malaria *Plasmodium berghei*, with live cell imaging, expansion, super-resolution, and electron microscopy, together with proteomic and conditional gene knockdown approaches, we show the association of NEK1 with a bipartite MTOC that spans the nuclear membrane during male gamete formation. NEK1 function is essential for MTOC organisation, spindle formation and kinetochore attachment, and hence male gamete formation. The absence of NEK1 blocks parasite transmission through the mosquito, with important implications for potential therapeutic strategies to control malaria.

Results

Plasmodium NEK1 has a punctate location, partially overlapping with the kinetochore and MTOC during blood stage schizogony

To study the expression and subcellular location of NEK1, we generated a transgenic parasite line by single crossover recombination at the 3' end of the endogenous *nek1* locus to express a C-terminal GFP-tagged fusion protein **(Fig S1A).** PCR analysis of genomic DNA using locus-specific diagnostic primers indicated correct integration of the GFP tagging construct **(Fig S1B).** Western blot showed NEK1-GFP protein expression of the correct size (~134 kDa) **(Fig S1C).** NEK1-GFP parasites completed the full life cycle, with no detectable phenotype resulting from the GFP tagging.

Live cell imaging was done using a NEK1-GFP line to study the location of NEK1 during various stages of parasite life cycle. Blood was collected from mice infected with NEK1-GFP parasites and incubated in schizont culture medium to analyse the location of NEK1 in parasite erythrocytic stages. NEK1-GFP was undetectable in

early stages (ring stages) by live cell imaging but was visible with a diffuse cytoplasmic location during later stages (trophozoites) **(Fig 1A)**. At the start of schizogony, NEK1-GFP re-located In the cytoplasm initially to single focal points near individual nuclei **(Fig 1A),** which later divided into two tightly associated punctae. A schematic of the first round of nuclear division during schizogony is portrayed at the top of Fig 1A, showing different mitotic components. The NEK1-GFP punctae splitting follows the subsequent asynchronous nuclear divisions. NEK1-GFP signal disappeared at the end of nuclear division and was undetectable in free merozoites **(Fig 1A)**.

To investigate further the subcellular location of NEK1, we compared its location with that of the kinetochore marker, NDC80. Parasite lines expressing NEK1-GFP and NDC80-mCherry were crossed, and the progeny were analysed by live-cell imaging to establish the spatiotemporal relationship of the two tagged proteins. The location of both NEK1-GFP and NDC80-mCherry was adjacent to the nuclear DNA, and with a partial overlap, although NDC80-mCherry was always closer to the DNA (**Fig 1B**). Next, we investigated NEK1-GFP co-localisation with centrin (MTOC marker) by indirect immunofluorescence assay (IFA), using antibodies to GFP and centrin, and schizonts fixed at different time points. We observed an overlap of NEK1 and centrin signals but in this case NEK1 was closer than centrin to the DNA (**Fig 1C**). Together, these data suggest that NEK1 is located close to the nuclear DNA, between the kinetochore, as marked by NDC80, and the MTOC, as marked by centrin. The location of NEK1-GFP was also studied during other asexual stages like liver schizogony and mosquito gut sporogony. The live cell images of the proliferative liver schizogony **(Fig S1D)** and sporogony **(Fig S1E)** stages showed similar patterns of NEK1-GFP foci formation during proliferative stages**.**

NEK1-GFP associates with MTOC formation and spindle dynamics during male gamete formation

NEK1-GFP expression in real-time was analysed by live cell imaging to visualise its spatiotemporal dynamics during the rapid mitoses of male gametogenesis. One minute after gametocyte activation, NEK1-GFP was detected at a single focal point in close proximity to the nucleus **(Fig 2A).** This focal point subsequently split in two with the two punctae moving to opposite sides of the nucleus within 3 minutes after

activation **(Fig 2A, B, Video S1).** These two NEK1-GFP foci then split again and moved to opposing sides of the nucleus (**Fig 2A, C, Video S2**). A third round of splitting producing eight NEK1-GFP foci at 8-10 minutes, coincident with the time taken for three rounds of mitosis **(Fig 2A)**. During exflagellation at the end of male gametogenesis, the NEK1-GFP signal was diffuse throughout the cytoplasm, then a single focal point re-appeared in each emerging male gamete **(Fig 2A).**

To better resolve the NEK1-GFP foci, 3D structured illumination microscopy (SIM) was used with fixed NEK1-GFP gametocytes (**Fig 2D, E**). This approach showed that by one minute after gametocyte activation, NEK1-GFP was present as two closely associated dumbbell-shaped structures at one side of the nuclear DNA (**Fig 2D**). Similar NEK1-GFP patterns were observed two to three minutes after activation of gametocytes showing dumbbell-shaped structures at opposite ends **(Fig 2D).**

To further examine the location of NEK1 during gametogenesis, we compared location of NEK1-mCherry with that of the outer cytoplasmic MTOC marker, centrin-4-GFP by live-cell imaging. Within 1 minute of gametocyte activation the NEK1-mCherry was observed as a single focal point, while the centrin-4-GFP was already divided in to two punctae, suggesting that centrin foci divide first followed by NEK1 (**Fig 2E**). Within 5-10 seconds NEK1-GFP also split and moved along with centrin-4 towards opposite ends of gametocyte (**Fig 2E**). At each pole, the NEK1-mCherry and centrin-4-GFP showed a significant overlap with Pearson's correlation coefficients (R-values) of 0.75, although NEK1-mCherry was generally positioned more towards the nucleus and centrin-4-GFP more towards the cytoplasm (**Fig 2E**).

We used Ultrastructure Expansion Microscopy (U-ExM) to further resolve the location of NEK1 during male gametocyte development. NEK1 was tagged at the C-terminus with a 3xHA tag generated using PlasmoGEM vectors and a recombineering strategy (https://plasmogem.umu.se/pbgem/). In non-activated microgametocytes, the bipartite MTOC, as highlighted by the NHS-ester (amino-reactive dye used for fluorescent labelling of protein density) and centrin staining, was visible spanning the nuclear membrane and linking the amorphous cytoplasmic part to the intranuclear body. At this stage, only a few sparse NEK1-HA punctate signals were visible in both cytoplasmic and nuclear part of MTOC **(Fig S2A)**. Thirty

seconds to one-minute post-activation, axonemes started to nucleate on the cytoplasmic side, as revealed by tubulin staining **(Fig 2F**). At this stage, NEK1-HA localised next to the centrin positive cluster of basal body and partially to the intranuclear spindle poles **(Fig 2F**). At one to two minutes post-activation, the cluster of basal bodies and spindle poles had separated and migrated towards the opposite side of the nucleus. At this stage, NEK1-HA form a link between the cluster of basal bodies and the spindle poles **(Fig S2A)**. From six to eight minutes post-activation, NEK1-HA was located around the basal bodies and spindle poles. The location of NEK1 at the connection between the basal bodies and spindle poles was also more marked **(Fig S2A).** By ten to twelve minutes, the NEK1-HA pattern at the MTOC overlapped that of the NHS-ester suggesting a pronounced connection between the basal body and the spindle pole **(Fig 2F**).

The U-ExM approach was also used with γ-tubulin to resolve further the location of NEK1-HA at the MTOC. As described previously, γ-tubulin re-locates from the cytoplasmic centriolar MTOC to spindle pole post-gametocyte activation (Rashpa and Brochet, 2022). In the period from one to ten minutes post-activation, NEK1-HA was located at the MTOC, as described above, enriched towards the cytoplasmic side of the acentriolar MTOC, while γ-tubulin was enriched towards the intranuclear side **(Fig S2B)**. Interestingly, a discrete region, apparent as a fine line across the acentriolar MTOC remained free both of NEK1-HA and γ-tubulin, which probably is the location of the ARK2 kinase as described below.

The spatiotemporal location of NEK1 with respect to kinetochore, spindle and axoneme markers during male gametogenesis

To assess more fully the association of NEK1 with the mitotic spindle during male gametogenesis, we compared its location in real time with that of kinetochore marker, NDC80 (Zeeshan et al., 2020), spindle microtubule plus-end binding protein, EB1 (Zeeshan et al., 2023), spindle-associated aurora kinase 2 (ARK2) (Zeeshan et al, 2023), and cytoplasmic axonemal protein, kinesin-8B (Zeeshan et al., 2019a). A parasite line expressing NEK1-GFP (green) was crossed with lines expressing mCherry (red) tagged NDC80, EB1, ARK2 or kinesin-8B, and progeny were examined by live-cell imaging to establish the spatiotemporal relationships of the tagged proteins.

Within 30 to 60 seconds after activation, both NEK1-GFP and NDC80-mCherry (kinetochore) appeared as focal points, close to but not overlapping each other and adjacent to the nuclear DNA **(Fig 3A, S3A).** Later, within 1-2 minutes after activation, the NEK1-GFP signal split into two strong focal points in the cytoplasm, while NDC80-mCherry extended to form a bridge-like structure within the nucleus **(Fig 3B, S3A, Video S3)**. After reaching the opposing sides of the nucleus, the two NEK1-GFP focal points remained stationary, while the NDC80-mCherry bridge was split and the signal retracted towards NEK1-GFP, forming two focal points adjacent to but not overlapping the NEK1-GFP signal. There were two further rounds of this splitting of NEK1-GFP and extension and rupture of NDC80-mCherry signal, resulting in eight focal points of NEK1 in the cytoplasm adjacent to NDC80 in the nucleus **(Fig 3A, S3A)** at the end of mitosis**.** A similar dynamic pattern of localisation was observed for NEK1-GFP with the nuclear spindle microtubule-associated protein, EB1-mCherry, which also formed an extended bridge **(Fig 3C, D, S3B).** These proteins were adjacent but did not overlap throughout male gametogenesis when EB1 was present at focal points (spindle poles) **(Fig 3C, S3B, Video S4)**. A similar pattern was observed with spindle-associated kinase, ARK2-mCherry; NEK1-GFP and ARK2-mCherry were in a similar location at spindle poles **(Fig 3E).** The NEK1-GFP signal was observed at the ends of ARK2-mCherry decorated extending spindles, but again with no overlap throughout male gametogenesis **(Fig 3E, F, S3C, Video S5).**

We next compared the spatiotemporal dynamics of NEK1-GFP with those of the basal body and axoneme protein, kinesin-8B-mCherry that localises in the cytoplasm(Zeeshan et al., 2019a). Live cell imaging showed that both NEK1 and kinesin-8B were located in the cytoplasm **(Fig 3G, S3D).** Within thirty to sixty seconds after activation, kinesin-8B appeared as a tetrad marking the basal bodies with NEK1 located in the middle of the kinesin-8B tetrad but extending more towards the nucleus **(Fig 3G)**. The duplication of both NEK1-GFP and kinesin-8B-mCherry-labelled tetrads occurred within 1 minute before the duplicates moved to opposite sides of the nucleus **(Fig 3H, S3D, Video S6).** In later stages, NEK1-GFP was duplicated two more times and remained associated with MTOCs, while kinesin-8B-mCherry had a distinct axonemal location in the cytoplasm **(Fig 3G, H, S3D).**

The dynamic spatiotemporal distribution of these proteins demonstrates that chromosome segregation and spindle dynamics in the nucleus (tagged with NDC80, ARK2 and EB1) and basal body/MTOC formation in the cytoplasm (tagged with kinesin-8B and NEK1) begin very early in gametogenesis, continuing in parallel and synchronously within different compartments of the male cell.

To investigate further at higher resolution the location of NEK1 with respect to the kinetochore, spindle and basal body, 3D-SIM was performed on fixed gametocytes expressing NEK1-GFP/NDC80-mCherry, NEK1-GFP/EB1-mCherry, NEK1-GFP/ARK2-mCherry, and NEK1-GFP/kinesin-8B-mCherry at one to two minutes post activation, when the first spindles had formed. Gametocytes expressing NEK1-GFP/NDC80-mCherry had elongated focal points of NEK1 in close vicinity to nucleus and punctate NDC80 labelled-kinetochores distributed across the nucleus to form a bridge **(Fig 3I).** There was no overlap between NEK1 and NDC80 but the beaded NDC80 signals (kinetochores) were aligned closely at the ends with dumbbell shaped NEK1 signals **(Fig 3I).** Similarly, the SIM images showed that EB1 and ARK2 were distributed on nuclear spindle microtubules with the elongated focal points of NEK1 close to the nucleus at both ends of the spindle and without any overlap with EB1 and ARK2 **(Fig 3J, K).** SIM images of gametocytes expressing kinesin-8B-mCherry and NEK1-GFP showed that their location was in the cytoplasm close to nucleus, with NEK1 located in the centre of kinesin-8B-marked tetrads but without any overlap **(Fig 3L).** The nonoverlapping NEK1 signal in the centre of cytoplasmic kinesin-8B tetrads suggest that the basal bodies are assembled at the outer MTOC in close proximity to the nucleus.

NEK1-GFP interacting proteins are components of the axoneme and flagellum

Next we aimed to identify putative proteins interacting with NEK1. We used a GFP-specific antibody to immunoprecipitate GFP-NEK1 and any associated proteins, from lysates of purified gametocytes prior to lysate preparation, the gametocytes had been activated for one to two min, when the mitotic spindles were fully extended to a bridge like structure, and cross-linked with 1% paraformaldehyde. The mild cross linking with formaldehyde helps to retain the loosely attached or indirectly interacting partners during the process of pull down. We analysed co-immunoprecipitates using a LC-MS/MS pipeline and performed enrichment analyses based on normalized

iBAQ values **(Fig 4).** We found three categories of proteins associated with NEK1: (1) DNA replication/repair, (2) cilium/flagellar/axoneme proteins (CFAPs), and (3) proteins of unknown function. Many of these conserved proteins are not annotated in PlasmoDB, but in-depth sequence/alphafold-guided searches and phylogenetic analyses revealed their homology with known ciliary and flagellar components **(Fig 4, Supplementary Table S1).** Due to variability between NEK1 pulldown replicates and within the controls, probably due to differences in precise timing of when samples were harvested at between 1 to 2 minutes post activation of gametocytes, we found only a few interactors meeting our strict significance thresholds (correction for multiple testing; false discovery rate (FDR)=5%). Interacting proteins meeting our criteria were: (I) the pre-replication complex subunit, CDC6 (PBANKA_1102900), (II) the CFAPs CFAP157 (PBANKA_0102700), CFAP73 (CCDC43; PBANKA_0934700), CFAP57 (PBANKA_1035700; WDR65) and the axoneme-associated kinesin-15 (PBANKA_1458800) and (III) two genes with unknown function LSA1 (PBANKA_1236600) and the putative lysine decarboxylase UIS14 (PBANKA_1003400). Despite the variability between replicates we found enrichment (albeit not significant) of additional replication, CFAP and some unknown proteins (**Fig4**): (i) additional members of the replication licensing machinery, CDC45 (PBANKA_0303300) and CDT1(PBANKA_1356300) **(Supplementary Table S1)**; (ii) subunits of the inner arm dynein (IAD) complex: DHC6 (PBANKA_0507300), DHC3 (PBANKA_1329200), DHC8 (PBANKA_0615700), DNAI1a/b (PBANKA_1428300; PBANKA_0822900), CFAP52/58/100/251 and RSP9/RSPH9 (radial spoke proteins: PBANKA_1109600; PBANKA_1431500) **(Fig 4, Supplementary Table S1)**; (iii) two kinases found in specific pulldowns, NDK (PBANKA_0104400), a nucleotide diphosphate kinase, and MORN (PBANKA_1405000), a MORN-containing phosphatidylinositol-4-phosphate 5-kinase. In human cells, these kinases are both associated with cilia (Hoff et al., 2018; Xu et al., 2016). Lastly, we found several candidate interactors, such as UIS25 (PBANKA_1320100), PBANKA_0719700, PBANKA_0102700, PBANKA_0811300, LSA1 (PBANKA_1236600) and UIS14 (PBANKA_ 1003400), which we suspect are likely involved in the axoneme **(Fig 4, Supplementary Table S1)**. Our data suggest a general association of NEK1 with axoneme/ciliary proteins as well as subunits of the replication machinery, although further experiments are needed to explore these interactions.

Conditional knockdown/depletion of NEK1 reveals an essential role during male gametogenesis

Our previous analysis of *P. berghei* protein kinases had suggested that NEK1 is likely to be essential for erythrocytic development (Tewari et al., 2010). Therefore, to examine the role of NEK1 during sexual stages, we had to use strategies that retained expression in blood stages but depleted the protein or transcript in sexual stages. We generated transgenic parasite lines to allow the conditional knockdown of NEK1 using either the auxin inducible degron (AID) for protein or the promoter trap double homologous recombination (PTD) systems for transcript depletion.

To generate the NEK1-AID parasite, the endogenous *nek1* gene was modified to express a protein tagged at the C-terminus with an AID/HA tag to degrade the fusion protein in the presence of auxin, in a line expressing the Tir1 protein (**Fig S4A).** Integration was confirmed by PCR **(Fig S4B)**. One hour of auxin treatment of mature gametocytes resulted in NEK1-AID/HA protein depletion **(Fig 5A, S4C),** which severely impaired male gamete formation in the form of exflagellation **(Fig 5B).** As observed by immunofluorescence, male gametocytes depleted of NEK1-AID/HA were unable to form the first mitotic spindles at one to two minutes post-activation; however, these cells still formed axonemes and underwent DNA replication (**Fig S4D**). Since NEKs are known to be required for centrosome separation in other eukaryotes (Fry et al., 2017; Quarmby and Mahjoub, 2005), we suggest that NEK1 might have a similar role during male gametogenesis.

To generate a P_{clag}*nek1* (NEK1clag) parasite line for transcript depletion, we used double homologous recombination to insert the cytoadherence-linked asexual protein (CLAG – PBANKA_1400600) promoter upstream of *nek1,* in a parasite line that constitutively expresses GFP (Janse et al, 2006) (**Fig S4E**), to take advantage of stage-specific expression of *clag* that is transcribed in blood stages but not in gametocytes (Sebastian et al., 2012). The correct integration was confirmed by diagnostic PCR (**Fig S4F**). Quantitative real time PCR (qRT-PCR) confirmed that *nek1* mRNA is downregulated by approximately 90% in these gametocytes **(Fig 5C, S4G)**. A phenotypic analysis of these *nek1*-knockdown parasites (NEK1clag) was then performed at different stages of parasite development within the mosquito.

Male gamete formation (exflagellation) was severely affected in NEK1clag compared to GFP (wild type) parasites (**Fig 5D**), and very few or no ookinetes (differentiated zygotes after fertilisation) were formed (**Fig 5E**). In mosquitoes fed NEK1clag parasites we observed no oocysts in the midguts, while hundreds of oocysts were present in comparable mosquitoes fed GFP wild type parasites (**Fig 5F, G**). To further confirm the absence of any oocyst or sporozoite, infected mosquitoes were allowed to feed on the naïve mice. Mosquitoes infected with *NEK1clag* parasites failed to transmit this parasite to susceptible mice, whilst mosquitoes were able to transmit the WT-GFP parasite at the same time, and blood stage infection was observed in naïve mice 4 days later **(Fig S4H).**

To determine the consequences of NEK1 knockdown on global mRNA transcription, we performed RNA-seq in duplicate on NEK1clag and WT-GFP gametocytes, 0 min and 30 min post-activation. All replicates were clustered together (**Fig S5A**) and totals of 72 to 115 million RNA-seq reads were generated per sample for the global transcriptome **(Fig S5B).** In both 0 min and 30 min activated gametocytes, *nek1* was significantly down-regulated (q value < 0.05, log2fold ≤1.5) in NEK1clag parasites compared to WT-GFP parasites (**Fig 5H, I**), thus confirming the qPCR result (**Fig 5C**). We observed little transcriptional perturbation in both 0 min and 30 min activated gametocytes likely relevant to the NEK1clag phenotype **(Supplementary Table S2).** Of the total perturbed genes, 117 and 201 were significantly down-regulated and 150 and 377 genes were significantly up-regulated in the NEK1clag parasites compared to WT-GFP controls in 0 min and 30 min activated gametocytes, respectively **(Supplementary Table S2).** Further gene-ontology (GO) based enrichment analysis revealed that some genes encoding kinases were differentially expressed in either or in both 0 min and 30 mins activated gametocytes (**Fig 5J**).

Next, we compared the proteomes and phosphoproteomes of NEK1-AID/HA gametocytes in the presence or absence of auxin at one to two minutes, 6 minutes and 12 minutes post-activation. No major differences were observed in the 1211 proteins that could be quantified and no NEK1 peptides were detected even in the absence of auxin. In the phosphopeptide-enriched fractions, we detected 5,269 phosphosites mapping to 1,627 proteins **(Supplementary Table S3)**. There was

better sample separation by biological replicate than by auxin treatment or time point, suggesting a high variability that we attributed to the auxin treatment. However, we identified ten phosphorylated peptides that were less abundant in the presence of auxin across at least two time points, including two NEK1 peptides, likely reflecting the protein depletion by auxin treatment **(Fig S5C)**. The other peptides were derived from four proteins of unknown function (PBANKA_0519900, PBANKA_0720000, PBANKA_0934900 and PBANKA_1320100): the minichromosome complex maintenance protein 2 (MCM2 - PBANKA_1024900); heat shock protein 90 (HSP90 - PBANKA_0805700); a putative calcyclin binding protein (PBANKA_1452600) and kinesin 15 (PBANKA_1458800) **(Fig S5C).**

Abnormal MTOC organization and kinetochore attachment following of conditional knockdown of NEK1 level.

We used U-ExM microscopy combined with antibody staining to study at high resolution the phenotype associated with NEK1-AID/HA depletion in male gametocytes, in particular the morphology of mitotic spindles. We compared non-activated and several stages of activated NEK1-AID/HA male gametocytes, in the presence or absence of auxin. Treated and non-treated non-activated male gametocytes were identical; the bipartite MTOC was observed with NHS ester and centrin staining towards the cytoplasmic side **(Fig S6).** In control male gametocytes activated for one to two minutes, the first mitotic spindle with associated spindle poles and basal bodies nucleating axonemes were observed both with NHS-ester and α/β-tubulin staining. However, upon depletion of NEK1-AID/HA by auxin treatment, the first mitotic spindle was not visible **(Fig S6)**, and NHS-ester and centrin staining indicated that the MTOC replicated. α/β-tubulin antibody staining further showed nucleating axonemes. However, the two pairs of MTOC had failed to clearly separate and were still linked by a structure that stains for NHS-ester but not for α/β-tubulin **(Fig S6)**. Additional NHS-ester staining bodies were visible in the nucleus **(Fig S6)**, which most likely corresponds to unattached kinetochores. In the absence of auxin, at ten to twelve minutes, the spindles of mitosis III had formed, with a single basal body attached to the eight spindle poles **(Fig 6A)**. In contrast, in NEK1-AID/HA depleted microgametocytes, the MTOC remained arrested as observed at 1-2 minutes post-activation and NHS-ester dots likely corresponding to free kinetochores were now clearly visible **(Fig S6)**. Despite the MTOC segregation

defects, axonemes had elongated but the majority were not bundled compared to those in parasites not treated with auxin **(Fig 6A)**.

To gain further high-resolution imaging, we performed transmission electron microscopy (TEM) analysis of NEK1clag and GFP-expressing wild type (WT-GFP) gametocytes at eight- and fifteen minutes post-activation. At eight minutes post-activation, many of the wildtype male gametocytes had progressed to the third genome division with multiple nuclear spindle poles within a central nucleus **(Fig 6Ba three arrow head).** In many cases, a basal body was visible, closely associated with and connected to the nuclear pole **(Fig 6Ba).** From the nuclear pole, nuclear spindle microtubules radiated into the nucleoplasm and connected to kinetochores **(Fig 6Bb).** Within the cytoplasm several elongated axonemes, some with the classical 9+2 microtubule arrangement, were visible **(Fig 6Bc).** The NEK1clag male gametocytes had a more spherical nucleus, and an extensive examination of over 200 male gametocytes failed to identify the presence of any nuclear poles or microtubules of mitotic spindles **(Fig 6Be)**. However, centrally located within the nucleus were several kinetochores either singly or in groups but with no evidence of microtubule attachment or nuclear pole formation **(Fig 6Bf, g).** Within the cytoplasm, it was possible to identify groups of basal bodies from which axonemes were formed, with a number exhibiting the classical 9+2 microtubule arrangement **(Fig 6Bh).** Like the WT, there appeared to be many partially or completely disorganized single and doublet microtubules.

At 15 minutes post-activation, many WT male gametocytes had undergone exflagellation, and there were several free male gametes. Exflagellation involves the extrusion of an axoneme and the associated nucleus of the male gamete **(Fig 6Bd),** leaving behind a residual male gametocyte consisting of a nucleus with small clumps of heterochromatin and cytoplasm of increased electron density containing a few residual microtubules. The male gametes consisted of the axoneme and a closely associated nucleus **(Fig 6Bd insert, e)** (Hair et al., 2023). In the NEK1clag parasite line at 15 minutes post-activation, many of the male gametocytes appeared to have also undergone some form of exflagellation with evidence of protrusion of axonemes **(Fig 6Bi)** and other microtubule combinations (not shown) from the surface of the male gametocyte but with no associated nucleus **(Fig 6Bi insert, j).** In an extensive search of over 250 randomly sectioned male gametes, only rarely was a nucleus

observed associated with an axoneme (<0.5%). This is in contrast with the observation of over 70% of axonemes with associated nucleus in randomly sectioned WT-GFP male gametes **(Fig 6Be)**. However, the residual male gametocytes were similar in appearance to the WT, although the NEK1 mutant appeared to have retained some disorganized kinetochores within the nucleus. Overall, the EM data revealed that NEK1 downregulation affected MTOC organisation, chromosome segregation and kinetochore attachment.

Discussion

NIMA-related protein kinases (NEKs) are a conserved family of proteins with an important role in mitosis (Fry et al., 2017; Oakley and Morris, 1983). The *Plasmodium* kinome encodes four NEK kinases. Two of them, NEK2 and NEK4, are not essential for parasite proliferation in the mammalian host, but one of them, NEK1, was found to be essential in blood stage proliferation (Solyakov et al., 2011; Tewari et al., 2010). Here, we have studied the location and function of NEK1 during the atypical modes of closed mitosis that presumably facilitate parasite proliferation in varied environments and coordinate MTOC biology, chromosome segregation, and axoneme formation. We chose to focus on the unconventional and rapid mitotic cell division that occurs during male gamete formation when three-fold genome replication takes place from 1N to 8N within 15 minutes, with formation of successive spindles within 8 min, and resulting in the formation of flagellated male gametes (Guttery et al., 2022; Sinden, 1983). This is also the stage of the centriole and de-novo basal body formation required for flagellum formation (Rashpa and Brochet, 2022; Sinden et al., 1978; Zeeshan et al., 2022a).

Our live cell imaging showed that NEK1-GFP has a discrete spatio-temporal location during asexual proliferation, largely restricted to schizogony, the stage when the parasite undergoes asynchronous endomitosis within red blood cells of the mammalian host. Distinct NEK1 foci were assembled, which were largely restricted to the periphery of the cytoplasm of the parasite cell, and partially co-localised with the outer cytoplasmic MTOC adjacent to the nucleus. The splitting of the NEK1 foci is reminiscent of the behaviour of human NEK2, which suggests that it may be functionally related and involved in MTOC splitting (Fry et al., 2017; Fry et al., 2012). Colocalisation adjacent to the kinetochore marker, NDC80, suggests that NEK localisation is coordinated with chromosome segregation during mitosis although the colocalisation was not precise. During male gametogenesis, this pattern was even clearer: the number and location of the NEK1 foci correlated with the ploidy of the parasite, and the splitting of the MTOC was observed associated with NEK1 foci at the different mitotic stages during genome replication from 1N to 8N (Fig 2A). The localisation of NEK1 in real time relative to a number of markers for kinetochores (NDC80) (Zeeshan et al., 2020), microtubules (EB1), spindle kinase (ARK2)(Zeeshan et al., 2023), and axoneme marker (Kinesin 8B) (Zeeshan et al.,

2019a), showed that NEK1 is part of the outer MTOC in the cytoplasmic compartment. This was confirmed by expansion microscopy and super resolution microscopy using various centrosome and spindle markers, including centrin, γ-tubulin and α-tubulin. A similar centrosomal location has been suggested for *Toxoplasma* NEK1 during mitosis in asexual proliferation (Chen and Gubbels, 2013; Suvorova et al., 2015), although our study is the first to examine its location during sexual stages in any apicomplexan parasite. This pattern of NEK1 location indicates that it is coordinated with outer cytoplasmic centriolar MTOC formation.

Previous functional studies suggested that *Plasmodium* NEK1 is likely be essential for *P. falciparum* and *P. berghei* asexual proliferation (Solyakov et al., 2011; Tewari et al., 2010). Here, we demonstrated a specific function for NEK1 during male gametogenesis using two different conditional knockdown systems. Using the AID system to degrade the protein or a promoter trap to downregulate the transcript, we show that male gamete formation was severely affected as measured by the exflagellation assay for male gamete formation. Studying this defect during the further developmental stages within the mosquito revealed that parasite transmission was completely blocked as no further development of the parasite was observed within the mosquito gut. This suggests that NEK1 has a crucial role during both the sexual stages and in parasite transmission, as found for other divergent kinases expressed during male gametogenesis, such as CDPK, SRPK and MAPK2, when similar results were obtained during our kinome gene knockout studies (Tewari et al., 2010), and also for other mitotic regulators, including CDC20 and APC3 (Guttery et al., 2012; Wall et al., 2018). These data also corroborate the phosphoproteomic studies of male gametogenesis in which NEK1 was shown to be associated with a specific cluster of phosphoregulation at this stage of development (Invergo et al., 2017). Global transcriptome analyses showed some differentially expressed kinases, although none was predicted to be involved in mitosis. Interestingly, while our phosphoproteomic analysis of NEK1-AID/HA gametocytes showed only limited changes, possibly due to the technical limitation of high variability between replicates, it highlighted kinesin-15 as being less phosphorylated following depletion of NEK1-AID/HA. As kinesin-15 was also enriched in NEK1-GFP immunoprecipitates, it is possible that the requirement for NEK1 may be to mediate phosphorylation of kinesin-15. Our recent systematic functional screen on kinesins

suggests the impairment of male gamete formation in kinesin-15 knockout parasites (Zeeshan et al., 2022b).

Our proteomic cross-linking studies provided additional interesting insights as most proteins bound to NEK1-GFP in the early stage of male gametogenesis, were likely proteins found in species with motile cilia (CFAPs) and proteins involved in DNA replication. Most notable were WDR16 (CFAP52), WDR65 (CFAP57), Kinesin-15, CFAP, RSP9 and several subunits of the inner arm dynein complex. Some of these, including Kinesin-8B and RSP9, have recently been shown to be involved in basal body and axoneme formation (Ramakrishnan et al., 2023; Zeeshan et al., 2019a). The connection with CDC6 and other replication-related proteins suggest that NEK1 is at some of the stages close to the chromatin, which is in agreement with a role of NEK1 in kinetochore/MTOC connection. All in all, many of the proteins in the NEK1-GFP pulldown, not least dynein, are involved in cilium or flagellum function (Kollmar, 2016).

Our U-ExM and electron microscopy analyses showed that NEK1 downregulation interfered with MTOC splitting, and ablated formation of the first mitotic spindle. In turn this prevented kinetochore attachment and led to impaired chromosome segregation. Many kinetochores were found distributed across the nucleus, suggesting a failure of chromosome attachment to the spindle from MTOC. Surprisingly, we could still see that some axonemes were made with 9+2 configuration, although only a few microgametes were produced, and these were devoid of a nucleus.

In summary, NEK1 forms discrete foci during proliferative stages in close vicinity to the nucleus with a significant overlap with centrosomal markers, such as γ-tubulin and centrin, and with partial overlap with the kinetochore marker NDC80. NEK1 interacts with centriolar and axonemal/flagellar proteins in gametocytes and its downregulation/depletion affects MTOC organization and splitting, spindle assembly and kinetochore attachment during male gametogenesis. The mechanism by which NEK1 contributes to MTOC splitting in *Plasmodium* remains to be elucidated.

Material and Methods

Ethics statement

The animal work performed in the UK passed an ethical review process and was approved by the United Kingdom Home Office. Work was carried out under UK Home Office Project Licenses (30/3248 and PDD2D5182) in accordance with the United Kingdom 'Animals (Scientific Procedures) Act 1986'. Six- to eight-week-old female CD1 outbred mice from Charles River laboratories were used for all experiments in the UK. All animal experiments performed in Switzerland were conducted with the authorisation numbers GE/82/15 and GE/41/17, according to the guidelines and regulations issued by the Swiss Federal Veterinary Office.

Generation of transgenic parasites

GFP-tagging vectors were designed using the p277 plasmid vector and transfected as described previously (Guttery et al., 2014a). A schematic representation of the wild type *nek1* locus (PBANKA_144300), the constructs and the recombined *nek1* locus can be found in **Fig S1A**. For GFP-tagging of NEK1 by single crossover homologous recombination, a region of *nek1* downstream of the ATG start codon was used to generate the construct. For the genotypic analyses, a diagnostic PCR reaction was performed as outlined in **Fig. S1A**. Primer 1 (intNEK1) and primer 2 (ol492) were used to determine correct integration of the *gfp* sequence at the targeted locus.

To study the function of NEK1, we used two conditional knock down systems: an auxin inducible degron (PP1AID) and a promoter exchange/trap using double homologous recombination (PP1PTD). The NEK1AID construct was derived from the p277 plasmid, where the GFP sequence was excised following digestion with *Age*I and *Not*I restriction enzymes and replaced with an AID/HA coding sequence. The AID-HA sequence was PCR amplified (using primers: 5'-CCCCAGACGTCGGATCCAATGATGGGCAGTGTCGAGCT-3' and 5'-ATATAAGTAAGAAAAACGGCTTAAGCGTAATCTGGA-3') from the GW-AID/HA plasmid (http://plasmogem.sanger.ac.uk/). Fragments were assembled following the Gibson assembly protocol to generate the NEK1-AID/HA transfection plasmid that was transfected in the 615 line. Conditional degradation of NEK1-AID/HA was

performed as described previously (Philip and Waters, 2015). A schematic representation of the endogenous *nek1* locus, the constructs and the recombined *nek1* locus can be found in **Fig S4A.** A diagnostic PCR was performed for *nek1* gene knockdown parasites as outlined in **Fig. S4A**.

The conditional knockdown construct NEK1clag was derived from *Pclag* (pSS368) where *nek1* was placed under the control of the clag promoter, as described previously (Sebastian et al., 2012). A schematic representation of the endogenous *clag* locus, the constructs and the recombined *clag* locus can be found in **Fig S4E**. A diagnostic PCR was performed for *nek1* gene knockdown parasites as outlined in **Fig S4E**. Primer 1 (5'-intPTD14) and Primer 2 (5'-intPTD) were used to determine successful integration of the targeting construct at the 5' end of the gene locus. Primer 3 (3'-intPTD) and Primer 4 (3'-intPTclag) were used to determine successful integration for the 3' end of the gene locus **(Fig S4F)**. All the primer sequences can be found in **Supplementary Table S4**. *P. berghei* ANKA line 2.34 (for GFP-tagging) or ANKA line 507cl1 expressing GFP (for the knockdown construct) parasites were transfected by electroporation (Janse et al., 2006).

Western blot analysis

Purified gametocytes were placed in lysis buffer (10 mM TrisHCl pH 7.5, 150 mM NaCl, 0.5 mM EDTA and 1% NP-40). The lysed samples were boiled for 10 min at 95 ºC after adding Laemmli buffer and then centrifuged at maximum speed (13000g) for 5 min. The samples were electrophoresed on a 4–12% SDS-polyacrylamide gel. Subsequently, resolved proteins were transferred to nitrocellulose membrane (Amersham Biosciences). Immunoblotting was performed using the Western Breeze Chemiluminescence Anti-Rabbit kit (Invitrogen) and anti-GFP polyclonal antibody (Invitrogen) at a dilution of 1:1250, according to the manufacturer's instructions.

Purification of schizonts and gametocytes

Blood cells obtained from infected mice (day 4 post infection) were cultured for 11h and 24 h at 37˚C (with rotation at 100 rpm) and schizonts were purified the following day on a 60% v/v NycoDenz (in PBS) gradient, (NycoDenz stock solution: 27.6% w/v NycoDenz in 5 mM Tris-HCl, pH 7.20, 3 mM KCl, 0.3 mM EDTA).

The purification of gametocytes was achieved by injecting parasites into phenylhydrazine treated mice (Beetsma et al., 1998) and enriched by sulfadiazine

treatment after 2 days of infection. The blood was collected on day 4 after infection and gametocyte-infected cells were purified on a 48% v/v NycoDenz (in PBS) gradient (NycoDenz stock solution: 27.6% w/v NycoDenz in 5 mM Tris-HCl, pH 7.20, 3 mM KCl, 0.3 mM EDTA). The gametocytes were harvested from the interface and activated.

Live cell imaging

To examine NEK1-GFP expression during erythrocyte stages, parasites growing in schizont culture medium were used for imaging at different stages (ring, trophozoite, schizont and merozoite) of development. Purified gametocytes were examined for GFP expression and localisation at different time points (0, 1-15 min) after activation in ookinete medium (Zeeshan et al., 2019b). Zygote and ookinete stages were analysed throughout 24 h of culture. Images were captured using a 63x oil immersion objective on a Zeiss Axio Imager M2 microscope fitted with an AxioCam ICc1 digital camera (Carl Zeiss, Inc).

Liver stage parasite imaging

For *P. berghei* liver stage parasites, 100,000 HeLa cells were seeded in glass-bottomed imaging dishes. Salivary glands of female *A. stephensi* mosquitoes infected with NEK1-GFP parasites were isolated and disrupted using a pestle to release sporozoites, which were pipetted gently onto the seeded HeLa cells and incubated at 37°C in 5% CO2 in complete minimum Eagle's medium containing 2.5 µg/ml amphotericin B (PAA). Medium was changed 3 h after initial infection and once a day thereafter. For live cell imaging, Hoechst 33342 (Molecular Probes) was added to a final concentration of 1 µg/ml, and parasites were imaged at 24, 48, 55 h post-infection using a Leica TCS SP8 confocal microscope with the HC PL APO 63x/1.40 oil objective and the Leica Application Suite X software.

Generation of dual tagged parasite lines

The NEK1-GFP parasites were mixed with either NDC80-cherry or EB1-mCherry or ARK2-mCherry or kinesin-8B-mCherry parasites in equal numbers and injected into mice. Mosquitoes were fed on mice 4 to 5 days after infection when gametocyte parasitaemia was high. These mosquitoes were checked for oocyst development and sporozoite formation at day 14 and day 21 after feeding. Infected mosquitoes

were then allowed to feed on naïve mice and after 4 - 5 days, and the mice were examined for blood stage parasitaemia by microscopy with Giemsa-stained blood smears. In this way, some parasites expressed both NEK1-GFP and NDC80-mCherry; or EB1-mCherry; or ARK2-mCherry; or kinesin-8B-mCherry in the resultant gametocytes, and these were purified, and fluorescence microscopy images were collected as described above.

Immunofluorescent assays (IFAs)

Immunofluorescent assays allowed for the characterisation of proteins in relation to NEK1-GFP, which had not been endogenously tagged with fluorescent proteins. Schizont smears were fixed with 2% paraformaldehyde in microtubule stabilising buffer (MTSB) on poly-L-lysine coated slides (Sigma). Slides were washed in Tris-buffered saline (1x TBS) before and after cell permeabilization using 0.1% Triton X100 in TBS, and subsequently blocked with a blocking solution consisting of 10% goat serum and 3% bovine serum albumin (BSA) in TBS. Primary antibodies consisting of rabbit polyclonal anti-GFP (1:250, Thermofisher) and mouse monoclonal anti-centrin (1:200, Sigma) were diluted in 1% BSA and 10 % goat serum in TBS and incubated on the slides for 1 hour. AlexaFluor 488 anti-rabbit (1:1000, green) and 568 anti-mouse (1:1000, red) (both Invitrogen; Table 4) secondary antibodies were also diluted in 1% BSA and 10 % goat serum in TBS and incubated in the dark for 45 minutes. Slides were washed with 1x TBS at the end of each incubation and were mounted in Vectashield with DAPI (Vector Labs) before being enclosed with a slip which was sealed with nail polish.

Structured illumination microscopy

Formaldehyde fixed (4%) gametocytes were stained for DNA with Hoechst dye and 2 µl of cell suspension was placed on microscope slide and covered with long (50x34mm) coverslip, to obtain a very thin monolayer and to immobilise the cells. Cells were scanned with an inverted microscope using Zeiss Plan-Apochromat 63x/1.4 Oil immersion or Zeiss C-Apochromat 63×/1.2 W Korr M27 water immersion objective on a Zeiss Elyra PS.1 microscope, using the structured illumination microscopy (SIM) technique. The correction collar of the objective was set to 0.17 for optimum contrast. The following settings were used in SIM mode: lasers, 405 nm: 20%, 488 nm: 16%, 561nm: 8%; exposure times 200 ms (Hoechst) 100 ms (GFP)

and 200ms (mCherry); three grid rotations, five phases. The band pass filters BP 420-480 + LP 750, BP 495-550 + LP 750 and BP 570-620 + 750 were used for the blue, green and red channels, respectively. Multiple focal planes (Z stacks) were recorded with 0.2 µm step size; later post-processing, a Z correction was done digitally on the 3D rendered images to reduce the effect of spherical aberration (reducing the elongated view in Z; a process previously tested with fluorescent beads 0.1µm, ThermoFisher T7284). Registration correction was also applied based on control images of multicolour fluorescent beads. Images were processed and all focal planes were digitally merged into a single plane (Maximum intensity projection). The images recorded in multiple focal planes (Z-stack) were 3D rendered into virtual models and exported as images and movies (see supplementary material). Processing and export of images and videos were done by Zeiss Zen 2012 Black edition, Service Pack 5 and Zeiss Zen 2.1 Blue edition.

Parasite phenotype analyses

Blood containing approximately 50,000 parasites of the WT-GFP and NEK1clag line was injected intraperitoneally (i.p.) into mice to initiate infections. Asexual stages and gametocyte production were monitored by microscopy on Giemsa-stained thin smears. Four to five days post infection, exflagellation and ookinete conversion were examined with a Zeiss AxioImager M2 microscope (Carl Zeiss, Inc) fitted with an AxioCam ICc1 digital camera(Guttery et al., 2012). To analyse mosquito transmission, 30–50 *Anopheles stephensi* SD 500 mosquitoes were allowed to feed for 20 min on anaesthetized, infected mice with an asexual parasitaemia of 15% and a comparable number of gametocytes as determined on Giemsa-stained blood films. To assess mid-gut infection, approximately 15 guts were dissected from mosquitoes on day 14 post feeding, and oocysts were counted on an AxioCam ICc1 digital camera fitted to a Zeiss AxioImager M2 microscope using a 63x oil immersion objective. Mosquito bite back experiments were performed 21 days post-feeding using naive mice, and blood smears were examined after 3-4 days.

Electron microscopy

Gametocytes activated for 8 min and 30 min were fixed in 4% glutaraldehyde in 0.1 M phosphate buffer and processed for electron microscopy (Ferguson et al., 2005). Briefly, samples were post fixed in osmium tetroxide, treated *en bloc* with uranyl

acetate, dehydrated and embedded in Spurr's epoxy resin. Thin sections were stained with uranyl acetate and lead citrate prior to examination in a JEOL JEM-1400 electron microscope (JEOL Ltd, UK).

Transcriptome study using RNA-seq

Total RNA was extracted from activated gametocytes and schizonts of WT-GFP and NEK1clag parasites (two biological replicates each) using RNeasy purification kit (Qiagen). RNA was vacuum concentrated (freeze dried) and transported using RNA-stable tubes (Biomatrica). Strand-specific 354 mRNA sequencing was performed on total RNA and using TruSeq stranded mRNA sample prep 355kit LT (Illumina) (Roques et al., 2019). Libraries were sequenced using an Illumina Hiseq 4000 sequencing platform with paired-end 150 bp read chemistry. The quality of the raw reads was assessed using FASTQC (http://www.bioinformatics.babraham.ac.uk/projects/fastqc). Low-quality reads and Illumina adaptor sequences from the read ends were removed using Trimmomatic R (Bolger et al., 2014). Processed reads were mapped to the *P. beghei ANKA* reference genome (release 40 in PlasmoDB - http://www.plasmoddb.org) using Hisat2 (Kim et al., 2015) (V 2.1.0) with parameter "—rna-strandness FR". Counts per feature were estimated using FeatureCounts (Liao et al., 2014). Raw read counts data were converted to counts per million (cpm) and genes were excluded if they failed to achieve a cpm value of 1 in at least one of the three replicates performed. Library sizes were scale-normalized by the TMM method using EdgeR software (Robinson et al., 2010) and further subjected to linear model analysis using the voom function in the limma package (Ritchie et al., 2015). Differential expression analysis was performed using DeSeq2 (Love et al., 2014). Genes with a fold-change greater than two and a false discovery rate corrected p-value (Benjamini-Hochberg procedure) < 0.05 were considered to be differentially expressed.

Quantitative Real Time PCR (qRT-PCR) analyses

RNA was isolated from gametocytes using an RNA purification kit (Stratagene). cDNA was synthesised using an RNA-to-cDNA kit (Applied Biosystems). Gene expression was quantified from 80 ng of total RNA using a SYBR green fast master mix kit (Applied Biosystems). All the primers were designed using the primer3 software (https://primer3.ut.ee/). Analysis was conducted using an Applied

Biosystems 7500 fast machine with the following cycling conditions: 95˚C for 20 s followed by 40 cycles of 95˚C for 3 s; 60˚C for 30 s. Three technical replicates and three biological replicates were performed for each assayed gene. The *hsp70* (PBANKA_081890) and *arginyl-t RNA synthetase* (PBANKA_143420) genes were used as endogenous control reference genes. The primers used for qPCR can be found in **Supplementary Table S4.**

Immunoprecipitation and Mass Spectrometry

Purified gametocytes were activated for 1.5- 2 min and were crosslinked using formaldehyde (10 min incubation with 1% formaldehyde, followed by 5 min incubation in 0.125M glycine solution and 3 washes with phosphate buffered saline (PBS) (pH, 7.5). Immunoprecipitation was performed using crosslinked protein and a GFP-Trap®_A Kit (Chromotek) following the manufacturer's instructions. Proteins bound to the GFP-Trap®_A beads were digested using trypsin and the peptides were analysed by LC-MS/MS. Briefly, to prepare samples for LC-MS/MS, wash buffer was removed, and ammonium bicarbonate (ABC) was added to beads at room temperature. We added 10 mM TCEP (Tris-(2-carboxyethyl) phosphine hydrochloride) and 40 mM 2-chloroacetamide (CAA) and incubation was performed for 5 min at 70° C. Samples were digested using 1 µg Trypsin per 100 µg protein at room temperature overnight followed by 1% TFA addition to bring the pH into the range of 3-4 before mass spectrometry. The tryptic peptides were analysed by liquid chromatography–tandem mass spectrometry. Mascot (http://www.matrixscience.com/) and MaxQuant (https://www.maxquant.org/) search engines were used for mass spectrometry data analysis. Experiments were performed in duplicate. Peptide and proteins having a minimum threshold of 95% were used for further proteomic analysis. The PlasmoDB database was used for protein annotation. iBAQ values for triplicate experiments for GFP-Nek1, GFP-SAS4 and a duplicate GFP-only were derived using Scaffold (https://www.proteomesoftware.com/products/scaffold-5). iBAQ values were normalized by the sum of all iBAQ values over one experiment. Only those proteins were considered with more than two unique peptides. See for details Table S1. Results were visualized using VolcaNoseR (ref: 10.1038/s41598-020-76603-3). Signficance of enrichment was assessed using the standard student T-test

(implemented in R). p-values were corrected for multiple testing using the Benjamini-Hochberg method.

Ultrastructure expansion microscopy

Sample preparation for U-ExM was performed as previously described (Rashpa and Brochet, 2022). Briefly, formaldehyde-fixed samples were attached to 12 mm round Poly-D-Lysine coated coverslips for 10 minutes. Coverslips were incubated for five hours in 1.4% formaldehyde (FA)/ 2% acrylamide (AA) at 37°C. Gelation was performed in ammonium persulfate (APS)/Temed (10% each)/Monomer solution (23% Sodium Acrylate; 10% AA; 0,1% BIS-AA in PBS) for 1 hour at 37°C. Gels were denatured for 90 minutes at 95°C. After denaturation, gels were incubated in distilled water overnight for complete expansion. The following day, gels were washed in PBS twice for 15 minutes to remove excess of water. Gels were then incubated with primary antibodies at 37°C for 3 hours and washed three times for ten minutes in PBS- 0.1% Tween. Incubation with secondary antibodies was performed for three hours at 37°C followed by three washes of ten minutes each in PBS- 0.1% Tween (all antibody incubation steps were performed with 120–160 rpm shaking at 37°C). Directly after antibody staining, gels were incubated in 1 ml of 594 NHS-ester (Merck: 08741) diluted at 10 µg/mL in PBS for one hour and 30 minutes at room temperature on a shaker. The gels were then washed three times for 15 minutes with PBS-Tween 0.1% and expanded overnight in ultrapure water. Gel pieces of 1cm x 1cm were cut from the expanded gel and attached on 24 mm round Poly-D-Lysine (A3890401, Gibco) coated coverslips to prevent gel from sliding and to avoid drifting while imaging. The coverslip was then mounted on a metallic O-ring 35mm imaging chamber (Okolab, RA-35-18 2000–06) and imaged. Images were acquired on Leica TCS SP8 microscope with HC PL Apo 100x/ 1.40 oil immersion objective in lightning mode to generate deconvolved images. System optimized Z stacks were captured between frames using HyD as detector. Images were processed with ImageJ, LAS X and Imaris 9.6 software.

Phosphoproteomic analysis

Sample preparation (SDS buffer-FASP procedure). Cell lysis was performed in 300 µl of 2% SDS, 25 mM NaCl, 50 mM Tris (pH 7.4), 2.5 mM EDTA and 20 mM TCEP supplemented with 1x Halt™ protease and phosphatase inhibitor. Samples

were vortexed and then heated at 95°C for 10 min with 400 rpm mixing on a thermomixer. DNA was sheared via four sonication pulses of 10 s each at 50% power. Samples were then centrifuged for 30 min at 17,000 g and the supernatant was collected. A Pierce protein assay was performed and a technical duplicate of the sample "- IAA 0 min" was generated. Three hundred µl samples were incubated with 48 µl of 0.5M iodoacetamide for 1h at room temperature. Protein was digested based on the FASP method (Wiśniewski et al.2009) using Amicon® Ultra-4, 30 kDa as centrifugal filter units (Millipore). Trypsin (Promega) was added at 1:80 enzyme/protein ratio and digestion performed overnight at room temperature. The resulting peptide samples were desalted with a Pierce™ Peptide Desalting Spin Column (Thermo Fisher Scientific) according to manufacturer's instruction and then completely dried under speed-vacuum.

TMTpro labelling procedure. Peptide concentration was determined using colourimetric peptide assay (Thermo Fisher Scientific). Briefly, 100 µg of each sample was labelled with 400 µg of one of the corresponding TMTpro reagents previously dissolved in 110 µl of 36% acetonitrile (CH_3CN), 200 mM EPPS (pH 8.5). Reaction was performed for 1h at room temperature and then quenched by adding hydroxylamine to a final concentration of 0.3% (v/v). Labelled samples were pooled together, dried and desalted with a Pierce™ Peptide Desalting Spin Column (Thermo Fisher Scientific) according to manufacturer's instruction and then completely dried under speed-vacuum.

Phosphopeptide enrichment. Phosphopeptides were enriched using High-Select Fe-NTA Phosphopeptide Enrichment Kit (Thermo Fisher Scientific) following manufacturer's instructions. Phosphopeptide fractions as well as the flow-through fraction were desalted with Pierce™ Peptide Desalting Spin Columns (Thermo Fisher Scientific) according to manufacturer's instruction and then completely dried under speed-vacuum.

ESI-LC-MS/MS. Peptide concentration was determined using a colorimetric peptide assay (ThermoFisher Scientific). All samples were reconstituted in loading buffer (5% CH_3CN, 0.1% formic acid [FA]) and 2 µg were injected into the column. LC-ESI-MS/MS was performed on an Orbitrap Fusion Lumos Tribrid mass spectrometer

(Thermo Fisher Scientific) equipped with an Easy nLC1200 liquid chromatography system (Thermo Fisher Scientific). Peptides were trapped on an Acclaim pepmap100, 3µm C18 , 75 µm x 20 mm nano trap-column (Thermo Fisher Scientific) and separated on a 75 µm x 500 mm, C18 ReproSil-Pur (from Dr. Maisch GmBH, 1.9 µm, 100 Å) home-made column. The analytical separation was run for 180 min using a gradient of 99.9% H_2O/0.1% FA (solvent A) and 80% CH_3CN/0.1% FA (solvent B). The gradient was run from 8 % to 28 % B in 160min, then to 40% B in 20 min then to 95 % B in 10 min with a final stay for 20 min at 95% B. Flow rate was 250 nL/min and total run time was 210 min. Data-Dependant Acquisition (DDA) was performed with MS1 full scan at a resolution of 120,000 FWHM followed by as many subsequent MS2 scans on selected precursors as possible within a 3 second maximum cycle time. MS1 was performed in the Orbitrap with an AGC target of 4 x 10^5, a maximum injection time of 50 ms and a scan range from 375 to 1500 m/z. MS2 was performed in the Orbitrap at a resolution of 50,000 FWHM with an AGC target at 5 x 10^4 and a maximum injection time of 86 ms. The isolation window was set at 0.7 m/z and 33% normalised collision energy was used for HCD. Dynamic exclusion was set to 60 s.

Database search. Raw data were processed using Proteome Discoverer (PD) 2.4 software (ThermoFisher Scientific). Briefly, spectra were extracted and searched against the *P. berghei* ANKA database (https://plasmodb.org/plasmo/app, release 10_2020, 5,076 entries) combined with an in-house database of common contaminants using Mascot (Matrix Science, London, UK; version 2.5.1). Trypsin was selected as the enzyme, with one potential missed cleavage. Precursor ion tolerance was set to 10 ppm and fragment ion tolerance to 0.02 Da. Carbamidomethylation of cysteine (+57.021) as well as TMTpro (+304.207) on lysine residues and on peptide N-termini were specified as fixed modifications. Oxidation of methionine (+15.995) as well as phosphorylation (+79.966) of serine, threonine and tyrosine were set as variable modifications. The search results were validated with Percolator. PSM and peptides were filtered with a false discovery rate (FDR) of 1%, and then grouped to proteins with a FDR of 1% and using only peptides with high confidence level. Both unique and razor peptides were used for quantitation. Protein and peptide abundance values were based on S/N values of reporter ions. Abundance was normalised on “Total Peptide Amount” and then scaled with “On all

Average". All the protein ratios were calculated from the medians of the summed abundances of replicate groups and associated p-values were calculated with ANOVA test based on the abundance of individual proteins or peptides.

Statistics and Reproducibility

All statistical analyses were performed using GraphPad Prism 9 (GraphPad Software). An unpaired t-test and two-way anova test were used to examine significant differences between wild-type and mutant strains for qRT-PCR and phenotypic analysis accordingly. For all experiments, biological replicates were defined as data generated from parasites injected into at least 3 mice.

Data Availability. The RNA-seq data generated in this study have been deposited in the NCBI Sequence Read Archive. The mass spectrometry proteomics data have been deposited to the ProteomeXchange Consortium

Author contributions.

RT conceived the study. RT, MZ, DB, GM performed the GFP tagging, live cell imaging and conditional knockdown with promoter trap experiments. RR and MB generated and characterised the NEK1-AID/HA line. MZ, GM, DB and RT performed protein pull-down experiments. RM and RT did 3D SIM imaging. ECT performed PCA analysis. RB and MR performed liver stage imaging. ARB performed mass spectrometry. RN, AS and AP performed RNA sequencing (RNA-seq). DJPF and SV performed electron microscopy. RT, MZ, RR, MB, AS, RN, AP, SLP and DJPF analyzed the data. MZ, and RT wrote the original draft. MZ, RT, AAH, AP, DJPF, RR, RN, MB, AMF, ECT, SLP edited and reviewed the manuscript and all other contributed to it.

Acknowledgments. This work was supported by: ERC advance grant funded by UKRI Frontier Science (EP/X024776/1), MRC UK (G0900278, MR/K011782/1, MR/N023048/1) and BBSRC (BB/N017609/1) to RT; the Francis Crick Institute (FC001097), the Cancer Research UK (FC001097), the UK Medical Research Council (FC001097), and the Wellcome Trust (FC001097) to AAH; the Swiss National Science Foundation project grant 31003A_179321 to MB. RN, AKS and AP are supported by a faculty baseline fund (BAS/ 1/1020-01-01) granted to AP by King

Abdullah University of Science and Technology (KAUST). This research was funded in whole, or in part, by the Wellcome Trust [FC001097]. For the purpose of Open Access, the author has applied a CC BY public copyright licence to any Author Accepted Manuscript version arising from this submission. DJPF and SV thank the Oxford Brookes Centre for Bioimaging for assistance.

Competing interests: The authors declare no competing interests.

Figure Legends

Fig 1. Location of NEK1 during asexual blood stage schizogony and its association with kinetochore (NDC80) and centrin.

A. The schematic on upper panel illustrates structures associated with mitosis during erythrocytic stage. Live cell imaging of NEK1-GFP (Green) showing its location during different stages of intraerythrocytic development and in a free merozoite. DIC: Differential interference contrast; Hoechst: stained DNA (blue); Merge: green and blue images merged; Guide: schematic of NEK1-GFP and nuclear DNA location at different stages of development. **B.** Live cell imaging of NEK1GFP (green) location in relation to the kinetochore marker NDC80-mCherry (red) and DNA (Hoechst, blue). Merge: green, red and blue images merged. Guide: schematic of NEK1, NDC80 and DNA location at three stages of schizogony. The dotted line indicates the periphery of the cell; the scale bar is 5 µm. **C.** Indirect immunofluorescence assays (IFAs) with centrin- and GFP-specific antibodies showing location of NEK1–GFP (green) in relation to centrin (red) and DNA (Hoechst, blue). Merge: green, red and blue images merged; inset shows higher magnification of nucleus in box in main panel. Guide: schematic of NEK1, Centrin and DNA location at three stages of schizogony. The dotted line indicates the periphery of the cell; the scale bar is 5 µm.

Fig 2. The location of NEK1, centrin and tubulin during basal body formation and axoneme assembly in male gametogenesis

A. Live-cell imaging of NEK1-GFP (green) during male gametogenesis showing foci in gametocytes at different time points after gametocyte activation and in the free male gamete (Flagellum). Panels are DIC, differential interference contrast, and merged, Hoechst (blue, DNA), NEK1-GFP (green). Scale bar = 5 µm. The guide

shows a schematic of gametogenesis with various structures indicated in both nucleus and cytoplasm. In the cytoplasm the centriolar MTOC has associated basal bodies and organises axoneme formation; adjacent in the nucleus the acentriolar MTOC has associated kinetochores. N refers to the ploidy of the cell. **B.** Stills from time lapse imaging showing split of NEK1-GFP focal point into two and their separation during the first round of mitosis at one to two minutes after gametocyte activation. Scale bar = 5 µm. **C.** Stills from time lapse imaging showing the split of NEK1-GFP and their separation during the second round of mitosis at three to four minutes after gametocyte activation. Scale bar = 5 µm. **D**. Super-resolution 3D-imaging of NEK1-GFP in gametocytes fixed at one and two to three minutes after activation. These are merged images of NEK1-GFP (green) and DNA (Hoechst, blue). The insets show a higher magnification of the boxed areas in the two panels. Scale bar = 1 µm. **E.** Live cell imaging showing location of NEK1-mCherry (red) in relation to centrin-4-GFP (green) in male gametocytes one to three minutes after activation. Pearson's correlation coefficient (R-value) for overlap between the NEK1 and centrin signals usually exceeded 0.75. Scale bar = 5 µm. **F.** Expansion microscopy showing location of NEK1-HA (yellow), centrin (blue) and α/β tubulin (magenta) detected with specific antibodies**.** Amine reactivity with NHS-ester is shown in shades of grey. The boxed areas in panels correspond to the zoomed insets. Axonemes: A; cMTOC: centriolar MTOC; aMTOC: acentriolar MTOC; spindle microtubules: MT. The guide illustrates NEK1 location relative to the MTOC. Scale bar = 5 µm.

Fig 3. The location of NEK1 in relation to kinetochore (NDC80), nuclear spindle (ARK2 and EB1), and basal body (kinesin-8B) markers during chromosome segregation in male gametogenesis

The guide illustrates structures associated with mitosis and axoneme formation. **A.** Live cell imaging showing the dynamics of NEK1-GFP (green) in relation to kinetochore marker (NDC80-mCherry [red]) at different time points during gametogenesis. DNA is stained with Hoechst dye (blue). Scale bar = 5 µm. **B.** Stills from time lapse imaging showing the dynamics of NEK1-GFP (green) in relation to kinetochore/spindle marker (NDC80-mCherry [red]) after one to two minutes activation**.** DNA is stained with Hoechst dye (blue). Scale bar = 5 µm. **C.** Live cell imaging showing the dynamics of NEK1-GFP (green) in relation to spindle marker

(EB1-mCherry [red]) at different time points during gametogenesis. DNA is stained with Hoechst dye (blue). Scale bar = 5 µm. **D.** Stills from time lapse imaging showing the dynamics of NEK1-GFP (green) in relation to spindle marker (EB1-mCherry [red]) after one to two minutes activation**.** DNA is stained with Hoechst dye (blue). Scale bar = 5 µm. **E.** Live cell imaging showing the dynamics of NEK1-GFP (green) in relation to spindle associated marker (ARK2-mCherry [red]) at different time points during gametogenesis. Scale bar = 5 µm. **F.** Stills from time lapse imaging showing the dynamics of NEK1-GFP (green) in relation to spindle associated marker (ARK2-mCherry [red]) after one to two minutes activation**.** DNA is stained with Hoechst dye (blue). Scale bar = 5 µm. **G.** Live cell imaging showing location of NEK1-GFP (green) in relation to the basal body and axoneme marker, kinesin-8B-mCherry (red) at different time points during gametogenesis. NEK1, like kinesin-8B, has a cytoplasmic location and remains associated with basal bodies during their biogenesis and axoneme formation throughout gamete formation. Scale bar = 5 µm. **H.** Stills from time lapse imaging showing the dynamics of NEK1-GFP (green) in relation to kinesin-8B-mCherry (red) after one to two minutes activation**.** DNA is stained with Hoechst dye (blue). Scale bar = 5 µm. **I.** Super-resolution 3D imaging of NEK1-GFP and NDC80-mCherry in gametocytes fixed at 1-2 min post activation. Scale bar = 1 µm. The inset is a higher magnification of the boxed area on the main panel; the guide is a cartoon of the cell. **J.** Super-resolution 3D imaging of NEK1-GFP and EB1-mCherry in gametocytes fixed at one to two minutes post activation. Scale bar = 1 µm. The inset is a higher magnification of the boxed area on the main panel; the guide is a cartoon of the cell. **K.** Super-resolution 3D imaging of NEK1-GFP and ARK2-mCherry in gametocytes fixed at one to two minutes post activation. Scale bar = 1 µm. The inset is a higher magnification of the boxed area on the main panel; the guide is a cartoon of the cell. **L.** Super-resolution 3D imaging of NEK1-GFP and kinesin-8B-mCherry in gametocytes fixed at one to two minutes post activation. Scale bar = 1 µm. The inset is a higher magnification of the boxed area on the main panel; the guide is a cartoon of the cell.

Fig 4. NEK1 co-immunoprecipitates with proteins involved in the axoneme assembly.

Fold enrichment (Log 2 transformed ratio) of normalized iBAQ values of proteins found in co-immunoprecipitates of NEK1-GFP versus control GFP. Multiple testing

correction was performed using the Hochberg method, setting the FDR at 5% meaning the initial p-value was set at 0.001 to conclude significant enrichment (red dotted lines). Additional proteins involved in the axoneme (CFAPs) that are enriched (2.25 times), but do not meet the significance criteria, are specifically indicated.

Fig 5. Knockdown/Depletion of NEK1 impairs male gamete formation and blocks parasite transmission

(A) NEK1-AID/HA protein expression levels visualised by western blotting following addition of auxin to mature purified gametocytes (+) or without (-) ; α-tubulin serves as a loading control. **(B)** Auxin (IAA) treatment of NEK1-AID/HA parasites abolished exflagellation (error bars show standard deviation from the mean; technical replicates from three independent infections) **(C)** qRTPCR analysis showing the downregulation of *NEK1* gene expression in *NEK1-Clag* parasites compared to WTGFP. Mean ± SEM, n=3 independent experiments. **(D)** Exflagellation centres per field at 15 min post-activation. n = 3 independent experiments (>20 fields per experiment). Error bar, ± SEM. **(E)** Percentage ookinete conversion from zygote. n= 3 independent experiments (> 100 cells). Error bar, ± SEM. **(F)** Mid guts at 10x and 63x magnification showing oocysts of *NEK1Clag* and WT-GFP lines at 14 days post infection (dpi). Scale bar=50 µM in 10x and 20 µM in 63x. **(G)** Total number of GFP-positive oocysts per infected mosquito in *NEK1Clag* compared to WT-GFP parasites at 14-day post infection. Mean ± SEM. n= 3 independent experiments. **(H, I).** Volcano plots showing significantly down-regulated (red, Log_2 fold ≤ −1, *q* value < 0.05) and up-regulated genes (green, Log_2 fold ≥1, *q* value < 0.05) in NEK1clag compared to wild-type lines in non (0 min)-activated gametocytes and 30 min activated gametocytes. **(J).** Expression heat map showing affected kinases.

Fig 6. Ultrastructural microscopy reveals a defect in MTOC organisation, spindle formation, and kinetochore attachment during male gametogenesis

A. Depletion of NEK1-AID upon auxin treatment blocks MTOC segregation as observed by U-ExM. α/β-Tubulin: magenta, centrin: blue, amine groups/NHS-ester reactive: shades of grey. Axonemes: A; cMTOC: centriolar MTOC; aMTOC: acentriolar MTOC; spindle microtubules: MT. Insets represent the zoomed area shown around centriolar and acentriolar MTOC highlighted by NHS-ester and/or

centrin staining. The additional NHS-ester punctate staining in the nucleus most likely correspond to detached kinetochores. The guide illustrates structures associated with mitosis and axoneme formation. Scale bars = 5 µm.

B. Electron micrographs of mid stage wild type (a – e) and NEK1 mutant (f – j) microgametocytes. Bar is 1 µm (a and f) and 200nm (b – e and g – j). **(a)** Low power image of a cross-sectioned microgametocyte showing a nucleus with three nuclear poles (arrows). Note the basal body (B) with attached axoneme (A) adjacent to one of the nuclear poles. **(b)** Detail of a nuclear pole (NP) with radiating microtubules (Mt) attached to kinetochores (K) with a basal body (B) in the adjacent cytoplasm. **(c)** Part of the cytoplasm showing cross section axonemes (A) illustrating 9+2 microtubular arrangement. **(d)** Part of an exflagellating microgamete showing the axoneme (A) and nucleus (N) still attached to the microgametocyte. **Insert**: Cross sectioned microgamete showing the nucleus (N) and axoneme (A). **(e)** Longitudinal section of a microgamete showing the axoneme (A) and nucleus (N). **(f)** Low power image of a mutant gametocyte showing the nucleus lacking any nuclear poles or spindles but with an array of kinetochore (K) in the central region. A number of axonemes (A) are present in the cytoplasm. **(g)** Detail of the central nuclear region showing four parallel arranged kinetochores (K). Note the absence of any microtubules attached to the kinetochores. **(h)** Part of the cytoplasm showing a cross sectioned axoneme (A). **(i)** Part of a gametocyte showing protrusion of an axoneme (A) to from a flagellum. Note the absence of any associated nucleus. **Insert:** Cross section flagellum (F) showing the presence of an axoneme but no nucleus. **(j)** Longitudinal section of a free flagellum (F) consisting of an axoneme but no nucleus.

Supplementary information

Supplementary Figures

Fig S1. Generation of PbNEK1-GFP parasites and analysis of subcellular location (A) Schematic representation of the endogenous *Pbnek1* locus, the GFP-tagging construct and the recombined *nek1* locus following single homologous recombination. Arrows 1 and 3 indicate the position of PCR primers used to confirm successful integration of the construct. **(B)** Diagnostic PCR of *nek1* and WT

parasites using primers IntNk1tg (Arrow 1) and ol492 (Arrow 3) to show the correct integration. Integration of the *nek1* tagging construct gives a band of 1400 bp. **(C)** Western blot showing the expression of endogenous NEK1 detected by ant-GFP antibody. **(D)** Live cell images showing the location of NEK1-GFP in liver stages. Scale bar = 5 µm. **(E)** Live cell images showing the location of NEK1-GFP during oocysts and sporozoite stages in mosquito. Scale bar = 5 µm. **(F)** Expansion microscopy of non-activated gametocytes showing location of NEK1-HA (yellow), centrin (blue) and α/β tubulin (magenta) detected with specific antibodies**.** Amine reactivity with NHS-ester is shown in shades of grey. The boxed areas in the second row of panels correspond to the insets in the bottom panels. Scale bar = 5 µm.

Fig S2. Location of NEK1-HA in relation to MTOC markers

A. Expansion microscopy showing location of NEK1-HA (yellow), centrin (blue) and α/β tubulin (magenta) detected with specific antibodies**.** Amine reactivity with NHS-ester is shown in shades of grey. The boxed areas in panels correspond to the zoomed insets. Axonemes: A; cMTOC: centriolar MTOC; aMTOC: acentriolar MTOC; spindle microtubules: MT. The guide illustrates NEK1 location relative to the MTOC. Scale bar = 5 µm. **B.** Expansion microscopy showing location of NEK1-HA (yellow), γ-tubulin (green) and α/β tubulin (magenta) stained with antibodies. Amine reactivity with NHS-ester is shown in shades of grey. The boxed areas in panels correspond to the zoomed insets. Axonemes: A; spindle microtubules: MT. Scale bar = 5 µm.

Fig S3. The location of NEK1 in relation to various subcellular markers (A) Live cell imaging showing the dynamics of NEK1-GFP (green) in relation to kinetochore marker (NDC80-mCherry [red]) at different time points during gametogenesis. **(B)** Stills from time lapse imaging showing the dynamics of NEK1-GFP (green) every 5 sec in relation to kinetochore/spindle marker (NDC80-mCherry [red]) after one to two minutes activation. **(C)** Live cell imaging showing the dynamics of NEK1-GFP (green) in relation to spindle marker (EB1-mCherry [red]) at different time points during gametogenesis. **(D)** Stills from time lapse imaging showing the dynamics of NEK1-GFP (green) every 5 sec in relation to spindle marker (EB1-mCherry [red]) after one to two minutes activation. (**E)** Live cell imaging showing the dynamics of

NEK1-GFP (green) in relation to spindle associated marker (ARK2-mCherry [red]) at different time points during gametogenesis. **(F)** Stills from time lapse imaging showing the dynamics of NEK1-GFP (green) every 5 sec in relation to spindle associated marker (ARK2-mCherry [red]) after one to two minutes activation. **(G)** Live cell imaging showing location of NEK1-GFP (green) in relation to the basal body and axoneme marker, kinesin-8B-mCherry (red) at different time points during gametogenesis. **(H)** Stills from time lapse imaging showing the dynamics of NEK1-GFP (green) every 5 sec in relation to kinesin-8B-mCherry (red) after one to three minutes activation. Scale bar = 5 µm.

Fig S4. Generation and genotypic analysis of *PbNEK1-AID/HA* and *NEK1clag* parasites. (A) Schematic representation of auxin inducible degron (AID) strategy to generate *NEK1-AID/HA* parasites. *goi*; gene of interest (nek1) (**B).** Integration PCR of the *NEK1-AID/HA* construct in the *ark2* locus. Oligonucleotides used for PCR genotyping are indicated, and agarose gels to analyse the corresponding PCR products from genotyping reactions are shown. (**C)** *NEK1-AID/HA* protein expression level as measured by western blotting using anti-HA antibodies upon addition of auxin to mature purified gametocytes; α-tubulin served as a loading control. **(D)** Immunofluorescence images of male gametocytes showing tubulin staining at different time points. DNA is stained with DAPI (blue). Scale bar = 1 µm. **(E)** Schematic representation of the promoter swap strategy to construct *NEK1clag* parasites (placing NEK1 under the control of the clag promoter) by double homologous recombination. Arrows 1 and 2 indicate the primer positions used to confirm 5' integration and arrows 3 and 4 indicate the primers used to confirm 3' integration. **(F)** Integration PCR of the promotor swap construct into the *NEK1* locus. Primer 1 (IntPTD14_5) and primer 2 (5'-IntPTD) were used to confirm successful integration of the selectable marker, resulting in a band of ~1500 bp. Primer 3 (3'-intPTclag) and primer 4 (IntPTD14_3) were used to determine the successful integration of the clag promoter, resulting in a band of ~750 bp. Primer 1 (IntPTD14_5) and primer 4 (IntPTD14_3) were used to confirm a complete knock-in of the construct with a band at ~4.7 kb and the absence of a band at ~1.3 kb. Representative image of more than 3 experiments. **(G)** qRT-PCR showing normalised expression of NEK1 transcripts in *NEK1clag* and WT-GFP parasites. Shown is mean ± SEM; n = 3 independent experiments. Student t test was used to

examine significant difference. ***p<0.01. **(H)** Graph showing prepatent period after bite back experiments. Shown is mean ± SEM; n = 3 independent experiments.

Fig S5. Transcriptomic and phosphoproteomics analysis of NEK1clag parasites (A) Clustered dendrogram of two biological replicates of WTGFP and NEK1clag mutant parasite lines during gametocyte stage (0 min and 30 min) using hierarchical clustering algorithm. Analysis was performed on normalized count data. **(B)** Table showing RNA-seq read statistics. **(C)** Volcano plots showing the extent of differentially phosphorylated peptides in gametocytes, comparing NEK1clag and WTGFP parasite lines.

Fig S6. Depletion of NEK1-AID upon auxin treatment blocks mitotic spindle formation. A. U-ExM images of non-activated gametocytes with and without depletion of NEK1-AID upon auxin treatment showing identical features highlighting α/β-Tubulin: magenta, centrin: blue, amine groups/NHS-ester reactive: shades of grey. white arrow: intra nuclear body, white insets represent the zoomed area shown around the basal body and MTOC. Scale bars = 5 µm. **B.** Depletion of NEK1-AID upon auxin treatment blocks mitotic spindle formation as observed by U-ExM. α/β-Tubulin: magenta, centrin: blue, amine groups/NHS-ester reactive: shades of grey. Axonemes: A; cMTOC: centriolar MTOC; aMTOC: acentriolar MTOC; spindle microtubules: MT. Insets represent the zoomed area shown around centriolar and acentriolar MTOC highlighted by NHS-ester and/or centrin staining. The additional NHS-ester punctate staining in the nucleus most likely correspond to detached kinetochores. Scale bars = 5 µm.

Supplementary Tables

Table S1. List of proteins and unique peptides values for GFP-trap immunoprecipitants.

Spreadsheet (excel) file with unique peptide values for GFP-trap immunoprecipitant for gametocytes 1.5 minute after activation for NEK1-GFP, WT-GFP (Negative control) and SAS4-GFP (Positive control) parasites. NAs are set to zero (0).

Table S2. List of genes differentially expressed between *NEK1clag* and WT-GFP gametocytes.

RNA sequencing analysis describing the expression pattern of various genes in *NEK1clag* gametocytes in comparison to WT-GFP gametocytes activated for 0 min and 30 min.

Table S3. List of phosphopeptides modulated in *NEK1clag* and WT-GFP gametocytes.

Table S4. Oligonucleotides used in this study.

Supplementary Movies

Supplementary Movie 1. Time lapse video showing NEK1-GFP (green) focal point splitting into two halves and moving apart in gametocytes 1 to 2 min after activation. Still images used in Fig 2B.

Supplementary Movie 2. Time lapse video showing NEK1-GFP (green) focal points splitting into four focal points and moving apart in gametocytes 3 to 4 min after activation. Still images used in Fig 2C.

Supplementary Movie 4. Time lapse video showing NEK1-GFP and NDC80-mCherry dynamics in gametocytes activated for 1 to 2 min. Still images used in Fig 3B.

Supplementary Movie 4. Time lapse video showing NEK1-GFP and EB1-mCherry dynamics in gametocytes activated for 1 to 2 min. Still images used in Fig 3D.

Supplementary Movie 5. Time lapse video showing NEK1-GFP and ARK2-mCherry dynamics in gametocytes activated for 1 to 2 min. Still images used in Fig 3F.

Supplementary Movie 6. Time lapse video showing NEK1-GFP and Kinesin-8B-mCherry dynamics in gametocytes activated for 1 to 2 min. Still images used in Fig 3H.

References

Arnot, D.E., Ronander, E., and Bengtsson, D.C. (2011). The progression of the intra-erythrocytic cell cycle of Plasmodium falciparum and the role of the centriolar plaques in asynchronous mitotic division during schizogony. Int J Parasitol *41*, 71-80.

Arquint, C., Gabryjonczyk, A.M., and Nigg, E.A. (2014). Centrosomes as signalling centres. Philos Trans R Soc Lond B Biol Sci *369*.

Avidor-Reiss, T., and Fishman, E.L. (2019). It takes two (centrioles) to tango. Reproduction *157*, R33-R51.

Bachus, S., Graves, D., Fulham, L., Akkerman, N., Stephanson, C., Shieh, J., and Pelka, P. (2022). In Mitosis You Are Not: The NIMA Family of Kinases in Aspergillus, Yeast, and Mammals. Int J Mol Sci *23*.

Beetsma, A.L., van de Wiel, T.J., Sauerwein, R.W., and Eling, W.M. (1998). Plasmodium berghei ANKA: purification of large numbers of infectious gametocytes. Exp Parasitol *88*, 69-72.

Bettencourt-Dias, M., and Glover, D.M. (2007). Centrosome biogenesis and function: centrosomics brings new understanding. Nat Rev Mol Cell Biol *8*, 451-463.

Bolger, A.M., Lohse, M., and Usadel, B. (2014). Trimmomatic: a flexible trimmer for Illumina sequence data. Bioinformatics *30*, 2114-2120.

Chen, C.T., and Gubbels, M.J. (2013). The Toxoplasma gondii centrosome is the platform for internal daughter budding as revealed by a Nek1 kinase mutant. J Cell Sci *126*, 3344-3355.

Dorin-Semblat, D., Schmitt, S., Semblat, J.P., Sicard, A., Reininger, L., Goldring, D., Patterson, S., Quashie, N., Chakrabarti, D., Meijer, L.*, et al.* (2011). Plasmodium falciparum NIMA-related kinase Pfnek-1: sex specificity and assessment of essentiality for the erythrocytic asexual cycle. Microbiology *157*, 2785-2794.

Dorin, D., Le Roch, K., Sallicandro, P., Alano, P., Parzy, D., Poullet, P., Meijer, L., and Doerig, C. (2001). Pfnek-1, a NIMA-related kinase from the human malaria parasite Plasmodium falciparum Biochemical properties and possible involvement in MAPK regulation. Eur J Biochem *268*, 2600-2608.

Ferguson, D.J., Henriquez, F.L., Kirisits, M.J., Muench, S.P., Prigge, S.T., Rice, D.W., Roberts, C.W., and McLeod, R.L. (2005). Maternal inheritance and stage-specific variation of the apicoplast in Toxoplasma gondii during development in the intermediate and definitive host. Eukaryot Cell *4*, 814-826.

Fry, A.M., Bayliss, R., and Roig, J. (2017). Mitotic Regulation by NEK Kinase Networks. Front Cell Dev Biol *5*, 102.

Fry, A.M., O'Regan, L., Sabir, S.R., and Bayliss, R. (2012). Cell cycle regulation by the NEK family of protein kinases. J Cell Sci *125*, 4423-4433.

Grallert, A., and Hagan, I.M. (2002). Schizosaccharomyces pombe NIMA-related kinase, Fin1, regulates spindle formation and an affinity of Polo for the SPB. EMBO J *21*, 3096-3107.

Guttery, D.S., Ferguson, D.J., Poulin, B., Xu, Z., Straschil, U., Klop, O., Solyakov, L., Sandrini, S.M., Brady, D., Nieduszynski, C.A.*, et al.* (2012). A putative homologue of CDC20/CDH1 in the malaria parasite is essential for male gamete development. PLoS Pathog *8*, e1002554.

Guttery, David S., Poulin, B., Ramaprasad, A., Wall, Richard J., Ferguson, David J., Brady, D., Patzewitz, E.-M., Whipple, S., Straschil, U., Wright, Megan H.*, et al.* (2014a). Genome-wide Functional Analysis of Plasmodium Protein Phosphatases Reveals Key Regulators of Parasite Development and Differentiation. Cell Host & Microbe *16*, 128-140.

Guttery, D.S., Poulin, B., Ramaprasad, A., Wall, R.J., Ferguson, D.J., Brady, D., Patzewitz, E.M., Whipple, S., Straschil, U., Wright, M.H.*, et al.* (2014b). Genome-wide functional analysis of Plasmodium protein phosphatases reveals key regulators of parasite development and differentiation. Cell Host Microbe *16*, 128-140.

Guttery, D.S., Zeeshan, M., Ferguson, D.J.P., Holder, A.A., and Tewari, R. (2022). Division and Transmission: Malaria Parasite Development in the Mosquito. Annu Rev Microbiol *76*, 113-134.

Hair, M., Moreira-Leite, F., Ferguson, D.J.P., Zeeshan, M., Tewari, R., and Vaughan, S. (2023). Atypical flagella assembly and haploid genome coiling during male gamete formation in Plasmodium. Nat Commun *14*, 8263.

Hoff, S., Epting, D., Falk, N., Schroda, S., Braun, D.A., Halbritter, J., Hildebrandt, F., Kramer-Zucker, A., Bergmann, C., Walz, G.*, et al.* (2018). The nucleoside-diphosphate kinase NME3 associates with nephronophthisis proteins and is required for ciliary function during renal development. J Biol Chem *293*, 15243-15255.

Invergo, B.M., Brochet, M., Yu, L., Choudhary, J., Beltrao, P., and Billker, O. (2017). Sub-minute Phosphoregulation of Cell Cycle Systems during Plasmodium Gamete Formation. Cell Rep *21*, 2017-2029.

Janse, C.J., Franke-Fayard, B., Mair, G.R., Ramesar, J., Thiel, C., Engelmann, S., Matuschewski, K., van Gemert, G.J., Sauerwein, R.W., and Waters, A.P. (2006).

High efficiency transfection of Plasmodium berghei facilitates novel selection procedures. Molecular and biochemical parasitology *145*, 60-70.

Kilmartin, J.V. (2014). Lessons from yeast: the spindle pole body and the centrosome. Philos Trans R Soc Lond B Biol Sci *369*.

Kim, D., Langmead, B., and Salzberg, S.L. (2015). HISAT: a fast spliced aligner with low memory requirements. Nature methods *12*, 357-360.

Kollmar, M. (2016). Fine-Tuning Motile Cilia and Flagella: Evolution of the Dynein Motor Proteins from Plants to Humans at High Resolution. Mol Biol Evol *33*, 3249-3267.

Li, J., Shami, G.J., Cho, E., Liu, B., Hanssen, E., Dixon, M.W.A., and Tilley, L. (2022). Repurposing the mitotic machinery to drive cellular elongation and chromatin reorganisation in Plasmodium falciparum gametocytes. Nat Commun *13*, 5054.

Liao, Y., Smyth, G.K., and Shi, W. (2014). featureCounts: an efficient general purpose program for assigning sequence reads to genomic features. Bioinformatics *30*, 923-930.

Liffner, B., Cepeda Diaz, A.K., Blauwkamp, J., Anaguano, D., Frolich, S., Muralidharan, V., Wilson, D.W., Dvorin, J.D., and Absalon, S. (2023). Atlas of Plasmodium falciparum intraerythrocytic development using expansion microscopy. Elife *12*.

Love, M.I., Huber, W., and Anders, S. (2014). Moderated estimation of fold change and dispersion for RNA-seq data with DESeq2. Genome Biol *15*, 550.

Mahjoub, M.R., Qasim Rasi, M., and Quarmby, L.M. (2004). A NIMA-related kinase, Fa2p, localizes to a novel site in the proximal cilia of Chlamydomonas and mouse kidney cells. Mol Biol Cell *15*, 5172-5186.

Moniz, L., Dutt, P., Haider, N., and Stambolic, V. (2011). Nek family of kinases in cell cycle, checkpoint control and cancer. Cell Div *6*, 18.

Morahan, B.J., Abrie, C., Al-Hasani, K., Batty, M.B., Corey, V., Cowell, A.N., Niemand, J., Winzeler, E.A., Birkholtz, L.M., Doerig, C.*, et al.* (2020). Human Aurora kinase inhibitor Hesperadin reveals epistatic interaction between Plasmodium falciparum PfArk1 and PfNek1 kinases. Commun Biol *3*, 701.

O'Connell, M.J., Krien, M.J., and Hunter, T. (2003). Never say never. The NIMA-related protein kinases in mitotic control. Trends Cell Biol *13*, 221-228.

Oakley, B.R., and Morris, N.R. (1983). A mutation in Aspergillus nidulans that blocks the transition from interphase to prophase. J Cell Biol *96*, 1155-1158.

Philip, N., and Waters, A.P. (2015). Conditional Degradation of Plasmodium Calcineurin Reveals Functions in Parasite Colonization of both Host and Vector. Cell Host Microbe *18*, 122-131.

Pradel, L.C., Bonhivers, M., Landrein, N., and Robinson, D.R. (2006). NIMA-related kinase TbNRKC is involved in basal body separation in Trypanosoma brucei. J Cell Sci *119*, 1852-1863.

Quarmby, L.M., and Mahjoub, M.R. (2005). Caught Nek-ing: cilia and centrioles. J Cell Sci *118*, 5161-5169.

Ramakrishnan, C., Fort, C., Marques, S.R., Ferguson, D.J.P., Gransagne, M., Baum, J., Chaouch, S., Mouray, E., Kohl, L., Wheeler, R.J.*, et al.* (2023). Radial spoke protein 9 is necessary for axoneme assembly in Plasmodium but not in trypanosomatid parasites. J Cell Sci *136*.

Rashpa, R., and Brochet, M. (2022). Expansion microscopy of Plasmodium gametocytes reveals the molecular architecture of a bipartite microtubule organisation centre coordinating mitosis with axoneme assembly. PLoS Pathog *18*, e1010223.

Reininger, L., Billker, O., Tewari, R., Mukhopadhyay, A., Fennell, C., Dorin-Semblat, D., Doerig, C., Goldring, D., Harmse, L., Ranford-Cartwright, L.*, et al.* (2005). A NIMA-related protein kinase is essential for completion of the sexual cycle of malaria parasites. J Biol Chem *280*, 31957-31964.

Reininger, L., Tewari, R., Fennell, C., Holland, Z., Goldring, D., Ranford-Cartwright, L., Billker, O., and Doerig, C. (2009). An essential role for the Plasmodium Nek-2 Nima-related protein kinase in the sexual development of malaria parasites. J Biol Chem *284*, 20858-20868.

Ritchie, M.E., Phipson, B., Wu, D., Hu, Y., Law, C.W., Shi, W., and Smyth, G.K. (2015). limma powers differential expression analyses for RNA-sequencing and microarray studies. Nucleic acids research *43*, e47.

Robinson, M.D., McCarthy, D.J., and Smyth, G.K. (2010). edgeR: a Bioconductor package for differential expression analysis of digital gene expression data. Bioinformatics *26*, 139-140.

Roques, M., Bindschedler, A., Beyeler, R., and Heussler, V.T. (2023). Same, same but different: Exploring Plasmodium cell division during liver stage development. PLoS Pathog *19*, e1011210.

Roques, M., Stanway, R.R., Rea, E.I., Markus, R., Brady, D., Holder, A.A., Guttery, D.S., and Tewari, R. (2019). Plasmodium centrin PbCEN-4 localizes to the putative MTOC and is dispensable for malaria parasite proliferation. Biol Open *8*.

Roques, M., Wall, R.J., Douglass, A.P., Ramaprasad, A., Ferguson, D.J., Kaindama, M.L., Brusini, L., Joshi, N., Rchiad, Z., Brady, D.*, et al.* (2015). Plasmodium P-Type Cyclin CYC3 Modulates Endomitotic Growth during Oocyst Development in Mosquitoes. PLoS Pathog *11*, e1005273.

Sebastian, S., Brochet, M., Collins, M.O., Schwach, F., Jones, M.L., Goulding, D., Rayner, J.C., Choudhary, J.S., and Billker, O. (2012). A Plasmodium calcium-dependent protein kinase controls zygote development and transmission by translationally activating repressed mRNAs. Cell Host Microbe *12*, 9-19.

Simon, C.S., Funaya, C., Bauer, J., Vobeta, Y., Machado, M., Penning, A., Klaschka, D., Cyrklaff, M., Kim, J., Ganter, M.*, et al.* (2021). An extended DNA-free intranuclear compartment organizes centrosome microtubules in malaria parasites. Life Sci Alliance *4*.

Sinden, R.E. (1983). Sexual development of malarial parasites. Adv Parasitol *22*, 153-216.

Sinden, R.E. (1991). Mitosis and meiosis in malarial parasites. Acta Leiden *60*, 19-27.

Sinden, R.E., Canning, E.U., Bray, R.S., and Smalley, M.E. (1978). Gametocyte and gamete development in Plasmodium falciparum. Proc R Soc Lond B Biol Sci *201*, 375-399.

Sinden, R.E., Talman, A., Marques, S.R., Wass, M.N., and Sternberg, M.J. (2010). The flagellum in malarial parasites. Curr Opin Microbiol *13*, 491-500.

Solyakov, L., Halbert, J., Alam, M.M., Semblat, J.P., Dorin-Semblat, D., Reininger, L., Bottrill, A.R., Mistry, S., Abdi, A., Fennell, C.*, et al.* (2011). Global kinomic and phospho-proteomic analyses of the human malaria parasite Plasmodium falciparum. Nat Commun *2*, 565.

Suvorova, E.S., Francia, M., Striepen, B., and White, M.W. (2015). A novel bipartite centrosome coordinates the apicomplexan cell cycle. PLoS Biol *13*, e1002093.

Tewari, R., Straschil, U., Bateman, A., Bohme, U., Cherevach, I., Gong, P., Pain, A., and Billker, O. (2010). The systematic functional analysis of Plasmodium protein kinases identifies essential regulators of mosquito transmission. Cell Host Microbe *8*, 377-387.

Voss, Y., Klaus, S., Guizetti, J., and Ganter, M. (2023). Plasmodium schizogony, a chronology of the parasite's cell cycle in the blood stage. PLoS Pathog *19*, e1011157.

Wall, R.J., Ferguson, D.J.P., Freville, A., Franke-Fayard, B., Brady, D., Zeeshan, M., Bottrill, A.R., Wheatley, S., Fry, A.M., Janse, C.J.*, et al.* (2018). Plasmodium APC3 mediates chromosome condensation and cytokinesis during atypical mitosis in male gametogenesis. Sci Rep *8*, 5610.

Wloga, D., Camba, A., Rogowski, K., Manning, G., Jerka-Dziadosz, M., and Gaertig, J. (2006). Members of the NIMA-related kinase family promote disassembly of cilia by multiple mechanisms. Mol Biol Cell *17*, 2799-2810.

Xu, Q., Zhang, Y., Wei, Q., Huang, Y., Hu, J., and Ling, K. (2016). Phosphatidylinositol phosphate kinase PIPKIgamma and phosphatase INPP5E coordinate initiation of ciliogenesis. Nat Commun *7*, 10777.

Zeeshan, M., Brady, D., Markus, R., Vaughan, S., Ferguson, D., Holder, A.A., and Tewari, R. (2022a). Plasmodium SAS4: basal body component of male cell which is dispensable for parasite transmission. Life Sci Alliance *5*.

Zeeshan, M., Ferguson, D.J., Abel, S., Burrrell, A., Rea, E., Brady, D., Daniel, E., Delves, M., Vaughan, S., Holder, A.A.*, et al.* (2019a). Kinesin-8B controls basal body function and flagellum formation and is key to malaria transmission. Life Sci Alliance *2*.

Zeeshan, M., Pandey, R., Ferguson, D.J.P., Tromer, E.C., Markus, R., Abel, S., Brady, D., Daniel, E., Limenitakis, R., Bottrill, A.R.*, et al.* (2020). Real-time dynamics of Plasmodium NDC80 reveals unusual modes of chromosome segregation during parasite proliferation. J Cell Sci *134*.

Zeeshan, M., Rashpa, R., Ferguson, D.J.P., Abel, S., Chahine, Z., Brady, D., Vaughan, S., Moores, C.A., Le Roch, K.G., Brochet, M.*, et al.* (2022b). Genome-wide functional analysis reveals key roles for kinesins in the mammalian and mosquito stages of the malaria parasite life cycle. PLoS Biol *20*, e3001704.

Zeeshan, M., Rea, E., Abel, S., Vukusic, K., Markus, R., Brady, D., Eze, A., Rashpa, R., Balestra, A.C., Bottrill, A.R.*, et al.* (2023). Plasmodium ARK2 and EB1 drive unconventional spindle dynamics, during chromosome segregation in sexual transmission stages. Nat Commun *14*, 5652.

Zeeshan, M., Shilliday, F., Liu, T., Abel, S., Mourier, T., Ferguson, D.J.P., Rea, E., Stanway, R.R., Roques, M., Williams, D.*, et al.* (2019b). Plasmodium kinesin-8X

associates with mitotic spindles and is essential for oocyst development during parasite proliferation and transmission. PLoS Pathog *15*, e1008048.

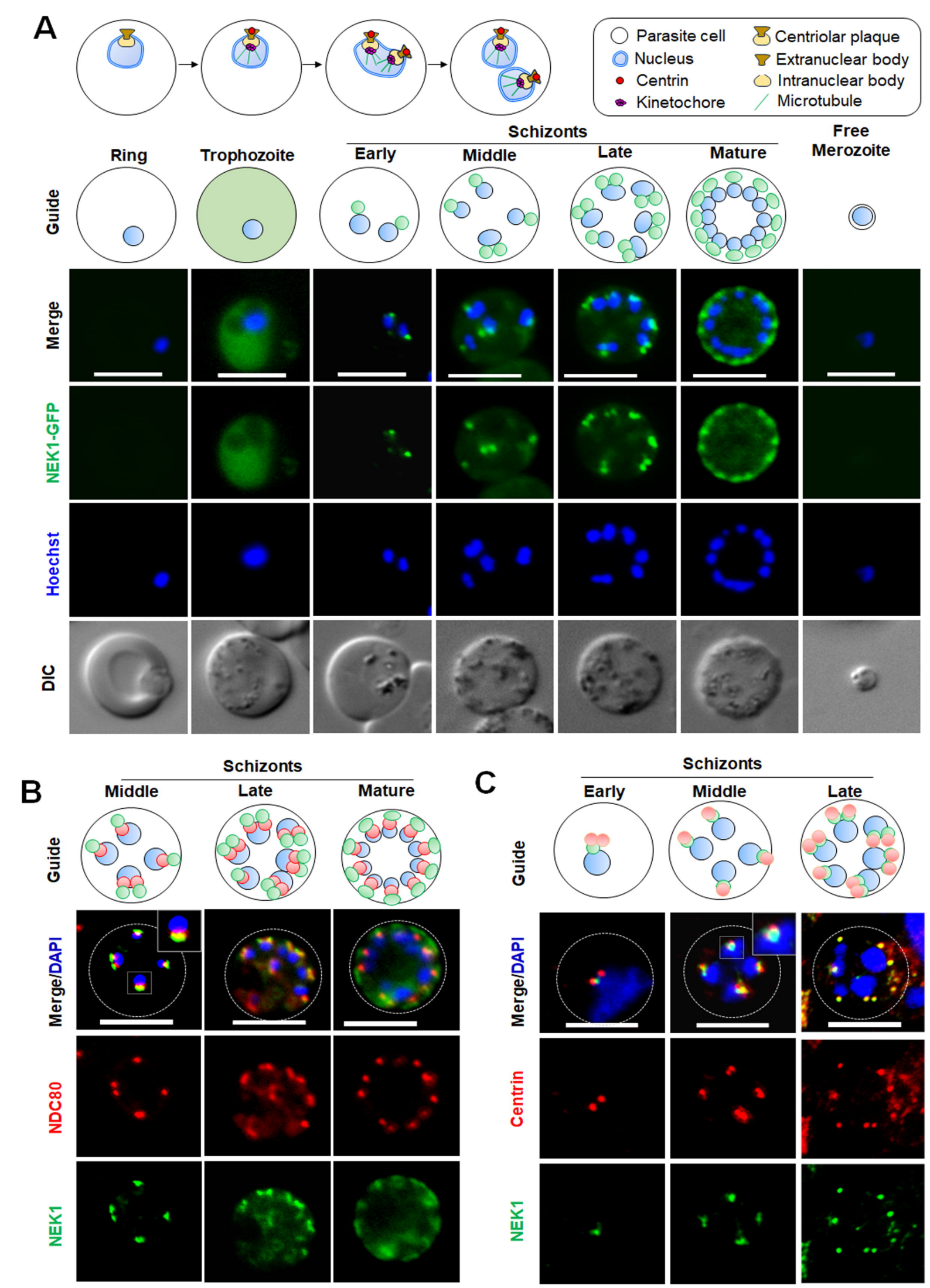
A
Parasite cell
Nucleus
Centrin
Kinetochore
Centriolar plaque
Extranuclear body
Intranuclear body
Microtubule
Schizonts
Ring
Trophozoite
Early
Middle
Late
Mature
Free Merozoite
Guide
Merge
NEK1-GFP
Hoechst
DIC
B
Schizonts
Middle
Late
Mature
Guide
Merge/DAPI
NDC80
NEK1
C
Schizonts
Early
Middle
Late
Guide
Merge/DAPI
Centrin
NEK1

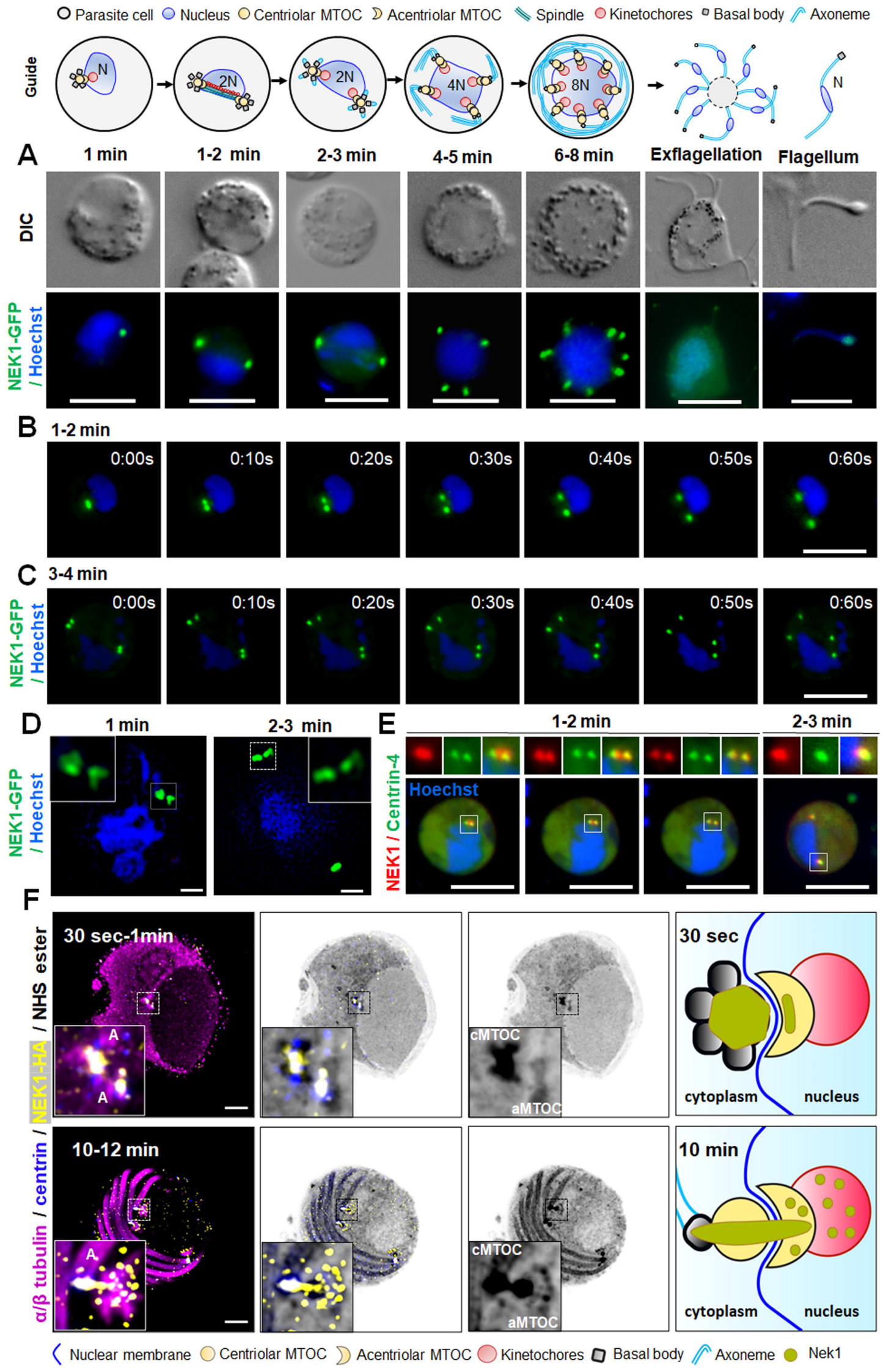
Parasite cell
Nucleus
Centriolar MTOC
Acentriolar MTOC
Spindle
Kinetochores
Basal body
Axoneme
Guide
N
2N
2N
4N
8N
N
A
1 min
1-2 min
2-3 min
4-5 min
6-8 min
Exflagellation
Flagellum
DIC
NEK1-GFP / Hoechst
B
1-2 min
0:00s
0:10s
0:20s
0:30s
0:40s
0:50s
0:60s
C
3-4 min
NEK1-GFP / Hoechst
D
1 min
2-3 min
NEK1-GFP / Hoechst
E
1-2 min
2-3 min
Hoechst
NEK1 / Centrin-4
F
30 sec-1min
NEK1-HA / NHS ester
A
cMTOC
aMTOC
30 sec
cytoplasm
nucleus
10-12 min
α/β tubulin / centrin
10 min
Nuclear membrane
Centriolar MTOC
Acentriolar MTOC
Kinetochores
Basal body
Axoneme
Nek1

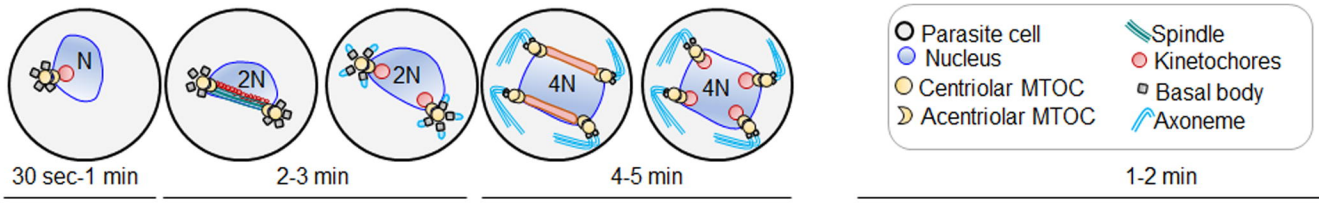
N
2N
2N
4N
4N
30 sec-1 min
2-3 min
4-5 min
1-2 min
Parasite cell
Nucleus
Centriolar MTOC
Acentriolar MTOC
Spindle
Kinetochores
Basal body
Axoneme

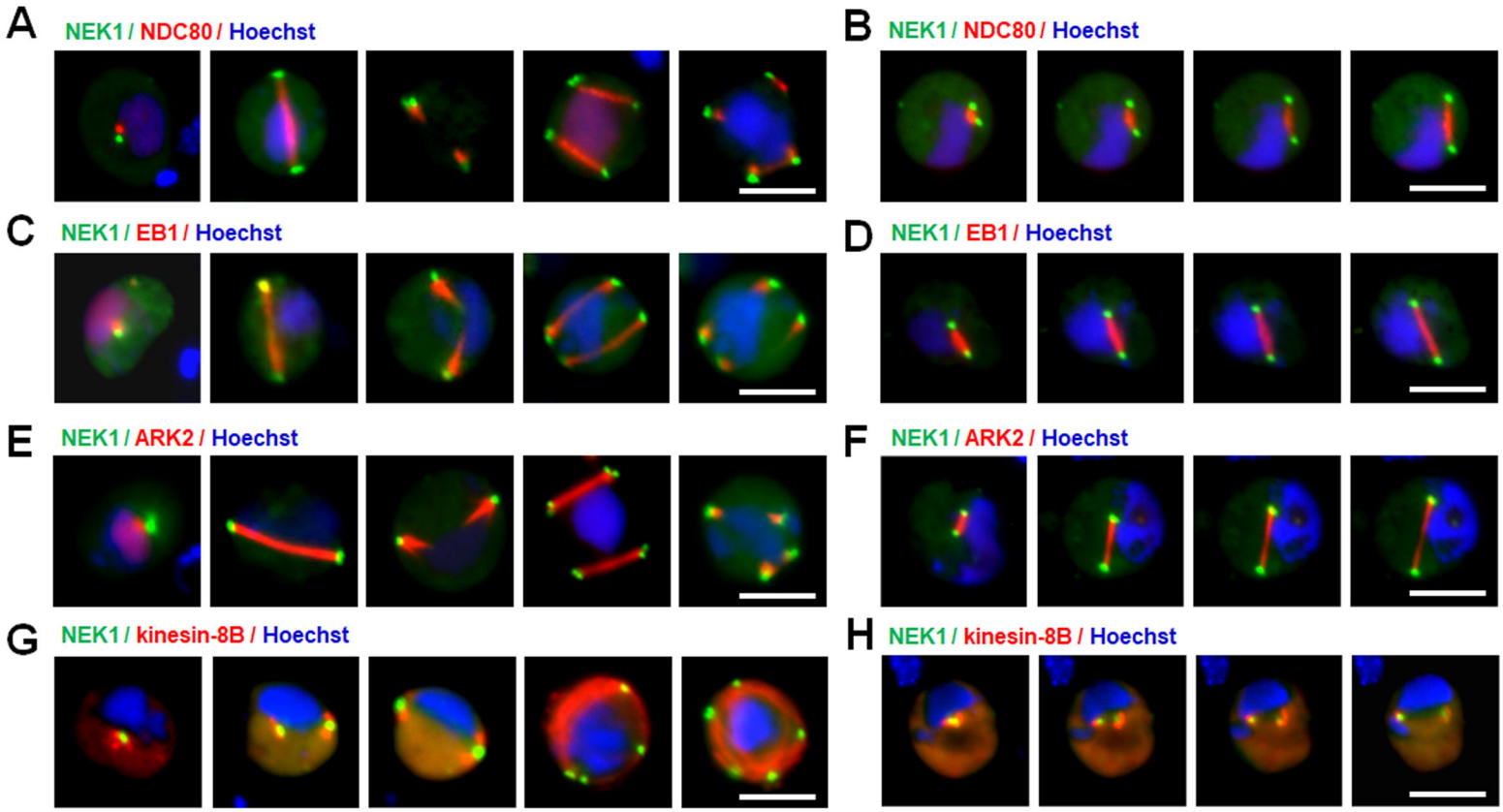
A
NEK1 / NDC80 / Hoechst
B
NEK1 / NDC80 / Hoechst
C
NEK1 / EB1 / Hoechst
D
NEK1 / EB1 / Hoechst
E
NEK1 / ARK2 / Hoechst
F
NEK1 / ARK2 / Hoechst
G
NEK1 / kinesin-8B / Hoechst
H
NEK1 / kinesin-8B / Hoechst

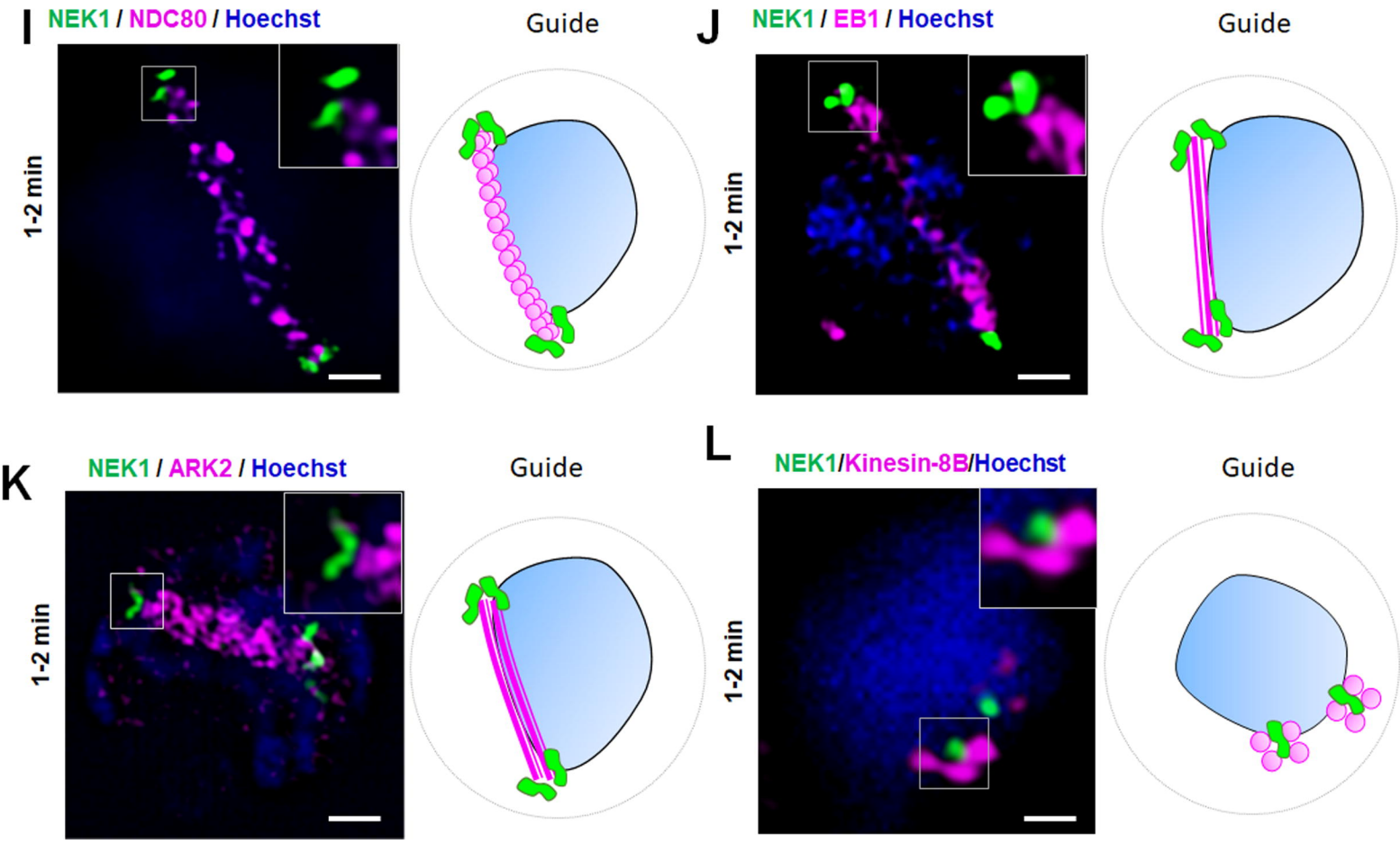
I
NEK1 / NDC80 / Hoechst
Guide
1-2 min
J
NEK1 / EB1 / Hoechst
Guide
1-2 min
K
NEK1 / ARK2 / Hoechst
Guide
1-2 min
L
NEK1/Kinesin-8B/Hoechst
Guide
1-2 min

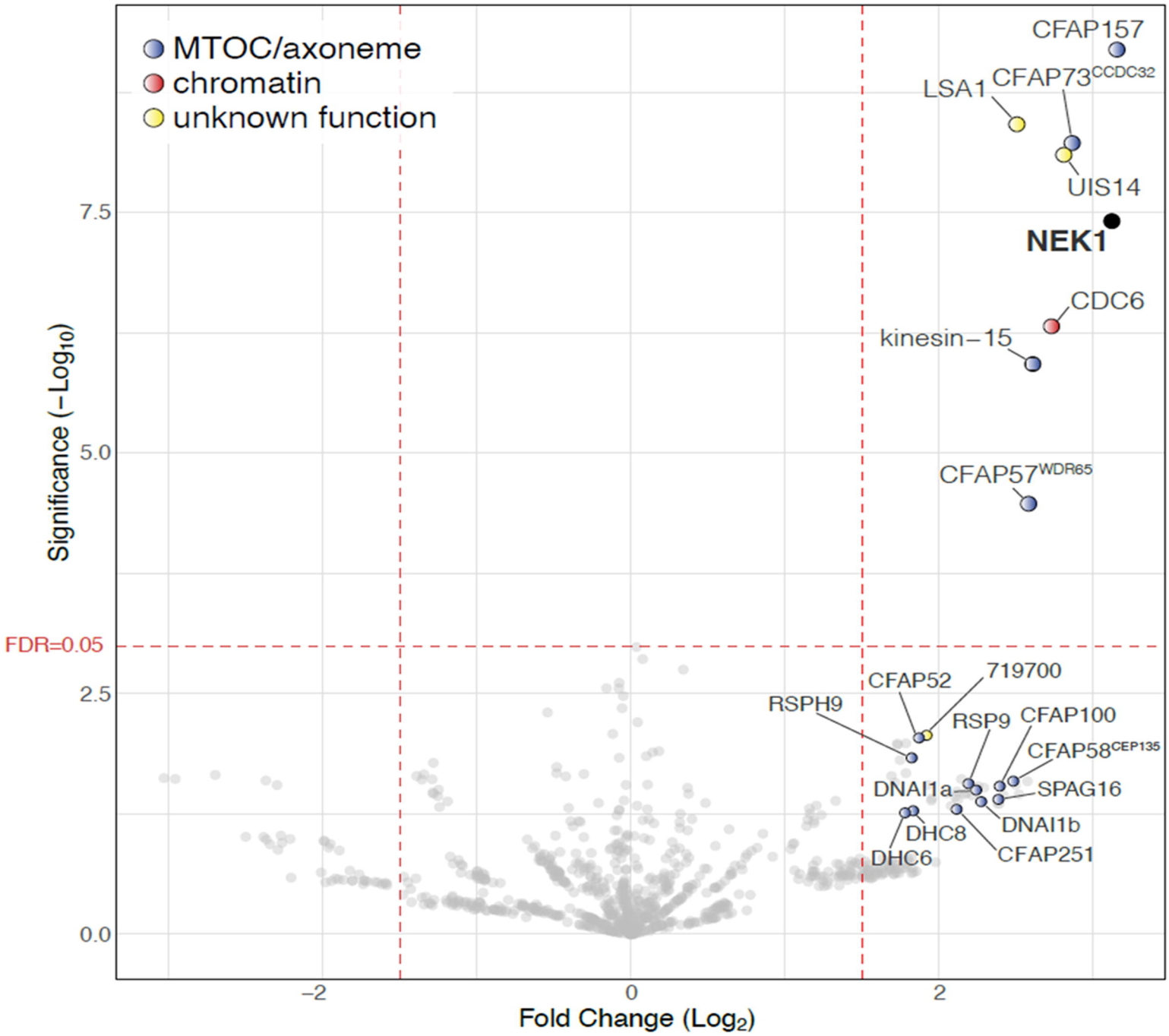
MTOC/axoneme
chromatin
unknown function
CFAP157
CFAP73CCDC32
LSA1
UIS14
NEK1
CDC6
kinesin−15
CFAP57WDR65
FDR=0.05
CFAP52
719700
RSPH9
RSP9
CFAP100
CFAP58CEP135
DNAI1a
SPAG16
DNAI1b
DHC8
DHC6
CFAP251
7.5
5.0
2.5
0.0
−2
0
2
Significance (−Log10)
Fold Change (Log2)

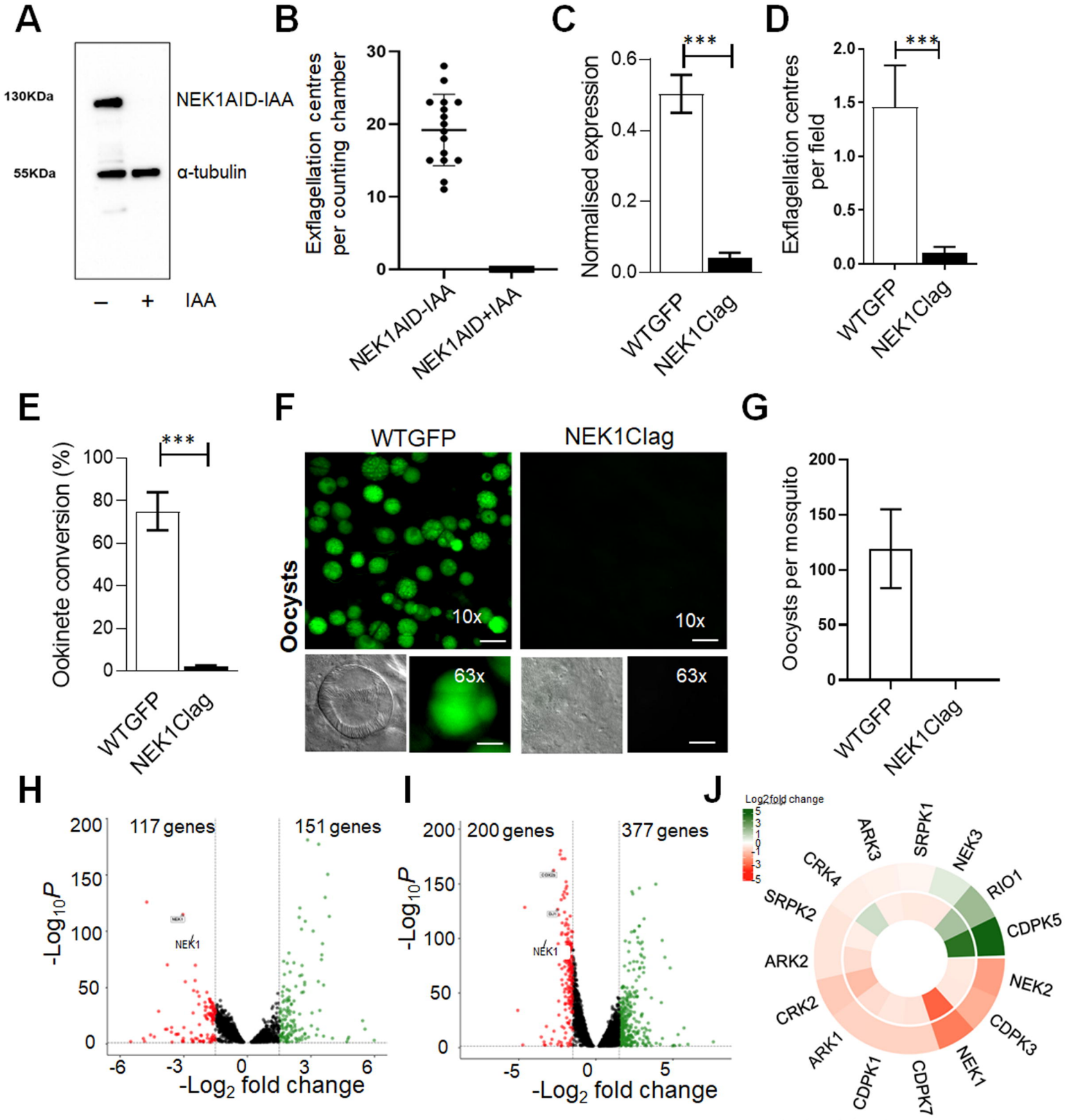
A
130KDa
55KDa
NEK1AID-IAA
α-tubulin
–
+
IAA
B
Exflagellation centres per counting chamber
30
20
10
0
NEK1AID-IAA
NEK1AID+IAA
C
Normalised expression
0.6
0.4
0.2
0.0
***
WTGFP
NEK1Clag
D
Exflagellation centres per field
2.0
1.5
1.0
0.5
0.0
***
WTGFP
NEK1Clag
E
Ookinete conversion (%)
100
80
60
40
20
0
***
WTGFP
NEK1Clag
F
WTGFP
NEK1Clag
Oocysts
10x
10x
63x
63x
G
Oocysts per mosquito
200
150
100
50
0
WTGFP
NEK1Clag
H
117 genes
151 genes
-Log10P
NEK1
-Log2 fold change
I
200 genes
377 genes
-Log10P
NEK1
-Log2 fold change
J
Log2fold change
ARK3
SRPK1
NEK3
RIO1
CDPK5
NEK2
CDPK3
NEK1
CDPK7
CDPK1
ARK1
CRK2
ARK2
SRPK2
CRK4

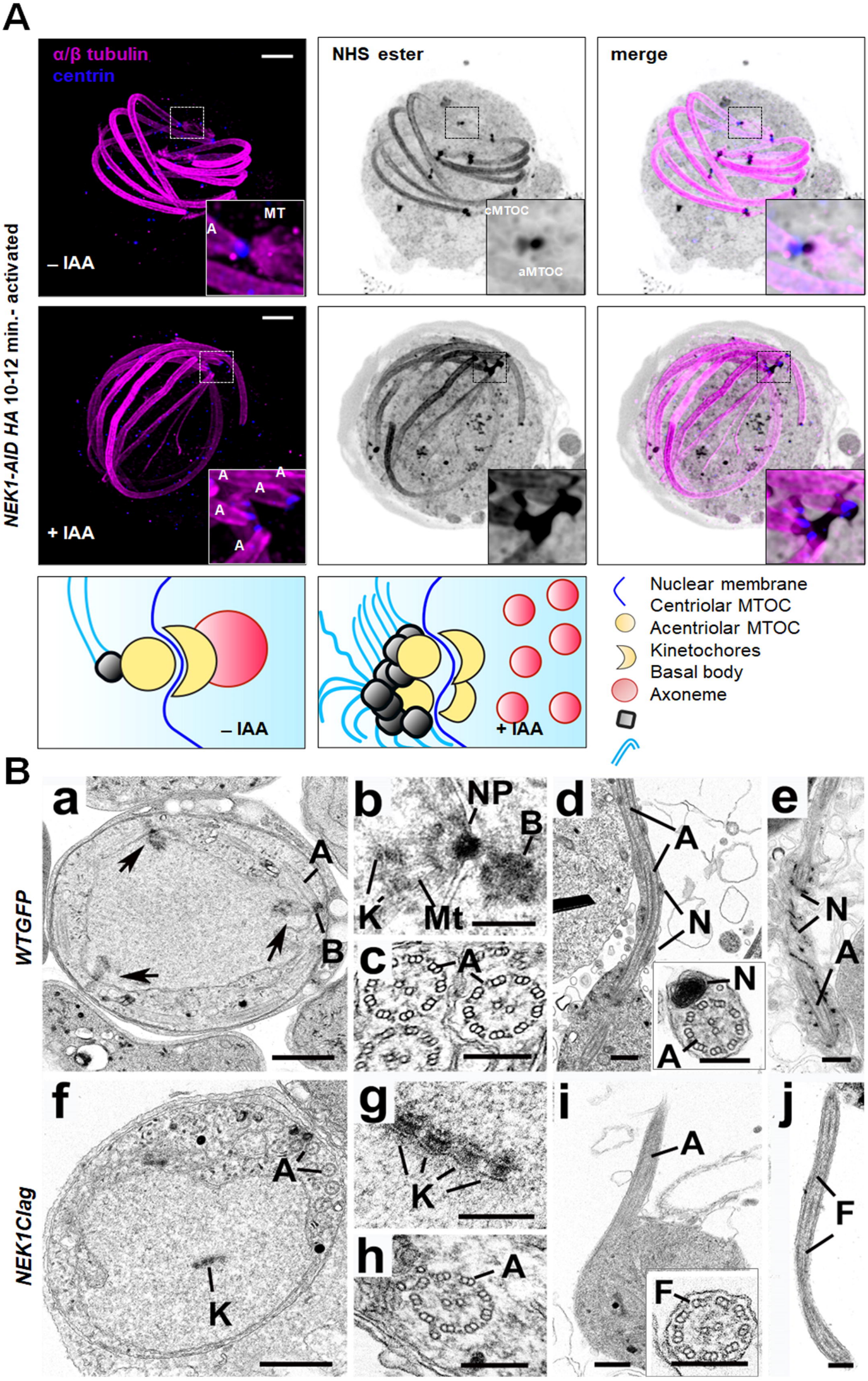
A
α/β tubulin
centrin
NHS ester
merge
MT
A
cMTOC
aMTOC
– IAA
+ IAA
NEK1-AID HA 10-12 min.- activated
Nuclear membrane
Centriolar MTOC
Acentriolar MTOC
Kinetochores
Basal body
Axoneme
B
WTGFP
NEK1Clag
a
b
c
d
e
f
g
h
i
j
NP
B
K
Mt
A
N
F